Red-shifted chemigenetic glutamate indicators for recording multiplexed neural computation

Nikki Tjahjono[1,2], Ji-You Min[2†], Julie A. Chouinard[2†], Philipe R.F. Mendonca[3†], Yihan Jin[2], Daigo Okada[2], Corinna S. Oswell[4], Hidehiko Inagaki[2], Eric R. Schreiter[5], Gregory Corder[4], Luke D. Lavis[5], Alessio Andreoni[2], Ehud Y. Isacoff[3*], Lin Tian[2,6,*]

[1] Biomedical Engineering Graduate Group, UC Davis; Davis, 95616, CA, USA

[2] Max Planck Florida Institute for Neuroscience; Jupiter, 33458, FL, USA

[3] Departments of Neuroscience and Molecular and Cell Biology, UC Berkeley; Berkeley, 94720, CA, USA

[4] Departments of Psychiatry, Anesthesiology and Critical Care, and Neuroscience, Perelman School of Medicine, University of Pennsylvania, Philadelphia, 19104, PA, USA

[5] Janelia Research Campus, Howard Hughes Medical Institute; Ashburn, 20147, VA, USA

[6] Lead contact

[†] These authors contributed equally

*Co-Corresponding authors. Lead contact: lin.tian@mpfi.org

SUMMARY

Neural computation relies on the integration of neurotransmitters, neuromodulators, and intracellular signal transduction. However, direct measurement of these interactions has been limited by spectral overlap among existing tools. Here, we introduce iHaloGluSnFR, the first family of chemigenetic glutamate sensors, permitting multiplexed optical measurement of excitatory neurotransmission alongside other neural signals. iHaloGluSnFR possesses tunable kinetics and glutamate affinities, and emission across red to far-red wavelengths. Using iHaloGluSnFR, we detected heterogeneous glutamate release profiles of boutons arising from a shared axonal arbor with quantal resolution, and identified spatially restricted coupling between calcium and transmitter release. We performed chronic *in vivo* recording of glutamate and dopamine dynamics during learning, revealing that learning selectively strengthens glutamate–dopamine coupling to encode motivational drive rather than reward consumption. Overall, iHaloGluSnFR provides a versatile chemigenetic toolkit for dissecting how chemical signals integrate across scales to regulate cellular communication, circuit computation, and adaptive behavior in the intact brain.

INTRODUCTION

Synaptic transmission is the foundation of information processing in the brain. Glutamate, the brain's principal excitatory neurotransmitter, plays a central role by mediating synaptic transmission, regulating synaptic plasticity and neuronal excitability, and for its roles in higher-order cognitive processes such as learning and memory. However, glutamatergic signaling does not occur in isolation: glutamate release and its postsynaptic effects are regulated by neuromodulators such as dopamine, acetylcholine, and serotonin, which dynamically reshape circuit properties and modulate temporal integration. Flexible behavior emerges from the combined action of these diverse inputs, which collectively shape how neurons transform synaptic activity into output. Dysfunction of glutamatergic transmission and neuromodulation have been implicated in neurodegenerative disorders for which the development of effective treatments has proven challenging, including Alzheimer's Disease, ALS, and Parkinson's Disease[1–5].

Genetically encoded glutamate indicators have transformed our understanding of excitatory transmission by enabling detection of glutamate release with cellular and subcellular precision in tissue and behaving animals[6–10]. However, understanding how synapses transform inputs into outputs requires simultaneous monitoring of glutamate alongside other neurochemicals. Most existing glutamate sensors are GFP- or YFP-based, creating substantial spectral overlap with widely used indicators for calcium and neuromodulators and confining experiments to sequential rather than simultaneous imaging. This spectral crowding limits our ability to relate glutamatergic input to postsynaptic calcium signals or to modulatory inputs in real time.

Expanding the glutamate sensor palette into the red and far-red spectral ranges is therefore essential. Although several red fluorescent protein–based sensors have been reported, their utility has been constrained by low brightness, small fluorescence changes, and blue-light–induced photoswitching[11–14]. Leveraging the brightness and spectral flexibility of chemigenetic indicators[15–18], we addressed the longstanding gap in red-shifted indicators by developing a suite of red and far-red chemigenetic glutamate sensors, iHaloGluSnFRs, optimized for spectral flexibility, broad dynamic

range, fast kinetics, and single vesicle sensitivity. iHaloGluSnFR reveals bouton-specific heterogeneity in glutamate release and short-term plasticity, enables spatially precise coupling of presynaptic calcium and glutamate in acute slices through dual-color two-photon imaging, and permits multiplexed *in vivo* fiber photometry recording with the green dopamine sensor dLight3.8 to uncover correlated yet distinct glutamate and dopamine dynamics during reward learning.

RESULTS

Engineering iHaloGluSnFR

iHaloGluSnFR was engineered by fusing the bacterial glutamate-binding protein GltI to circularly permuted HaloTag7 (cpHalo)[18] (**Figure 1A**), which enables rapid and specific covalent labeling with red and far-red Janelia Fluor (JF) dye-ligands[19–21]. The initial prototype (V0), labeled with JF635[19], showed a ~150% fluorescence increase upon glutamate addition (**Figure S1A**), indicating that GltI's ligand-induced conformational change modulates the dye's spirolactone–zwitterion equilibrium (**Figure 1A**). To improve sensor performance, we established a semi-automated, mammalian cell-based sensor screening and image analysis pipeline for iterative mutagenesis of iHaloGluSnFR bound to JF635 (**Figures 1B and S1B**). Linker optimization and addition of the V180S hinge mutation[10] produced a higher-affinity (EC50) sensor, V2 (**Figures 1C and S1B-C**). Subsequent screening of ~900 interface and linker variants led to two high dynamic range (E_{max}) sensors, V2.6 and V2.7b (**Figures 1C and S1B, D**).

To characterize the intrinsic properties of these variants, we engineered HEK293T cell lines stably expressing the sensors fused to Cobl9 GPI for extracellular plasma membrane localization[7]. *In situ* titration of glutamate showed that, when bound to JF635, sensitivity, represented by the S-slope, trended as V2>V2.6>V2.7b, while dynamic range trended as V2.7b>V2.6>V2 (V2-JF635: E_{max}=203.9± 5.9%, EC50=1.1 ± 0.2 μM, S-slope=185 uM^{-1}; V2.6-JF635: E_{max}=720.8± 45.2%, EC50=12.4 ± 3.3 μM, S-slope=58 uM^{-1}; V2.7b-JF635: E_{max}=1470± 117%, EC50=84.6 ± 25.2 μM, S-slope=17 uM^{-1}; **Figure 1D and Table S1**).

With JF585 and JF646, different sensor-dye combinations yielded shifts in sensitivity while preserving each dye's native excitation and emission spectra[19] (**Figures 1E-F and S1E**). JF585 increased the sensitivity of high dynamic range variants V2.6 and V2.7b relative to JF635 (**Figures 1E and S1F-H**), albeit with reduced $\Delta F/F_0$, while all variants showed robust but lower responses when labeled with JF646 (**Figures 1F and S1F-H**) (V2-JF585: E_{max}= 25.2± 3.9%, EC50= 978±906 nM, S-slope= 26 uM^{-1}; V2.6-JF585: E_{max}= 143.6± 9.5%; EC50= 0.77 ± 0.3 μM, S-slope=187 uM^{-1}; V2.7b-

JF585: E_{max}= 331.9± 11.3%, EC50= 6.2 ± 1.2 μM, S-slope= 54 uM^{-1}; V2-JF646: E_{max}= 14.0± 2.0%; V2.6-JF646: E_{max}= 164.4± 9.4%; V2.7b-JF646: E_{max}= 161.5± 8.4%; **Table S1**).

To compare per-molecule brightness across sensor versions, we engineered HEK239T stably expressing Citrine-fused sensors[22] (**Figure 1G-I**). Across all dyes, V2 displayed the highest apo-state molecular brightness, while V2.6 appeared brightest upon 200 μM glutamate addition (**Figure 1G-I**). We confirmed that iHaloGluSnFR is highly specific for glutamate, displaying no detectable responses to other neurotransmitters and lower affinity and responses to aspartate (**Figure S1I-J**).

iHaloGluSnFR displayed tunable spectra and kinetics in dissociated neuronal culture and acute brain slice with two-photon imaging

In cultured hippocampal neurons labeled with JF585 or JF635, iHaloGluSnFR variants showed EC50 and maximum $\Delta F/F_0$ trends consistent with performance in HEK293T cells (**Figure S2A-B**). We next assessed the sensitivity of iHaloGluSnFR to detect neuronal glutamate release triggered by electrical stimuli (**Figure 2A-C**). With JF635, V2.6 exhibited the largest response to a single electrical pulse (V2: $\Delta F/F_0$= 6.7 ± 0.9%, V2.6: $\Delta F/F_0$= 10.9± 1.4%, V2.7b: $\Delta F/F_0$ = 6.0 ± 1.7%), V2.7b exhibited the fastest decay (V2: $t_{1/2}$= 642 ± 60.6 ms, V2.6: $t_{1/2}$ = 86.0 ± 14.4 ms, V2.7b: $t_{1/2}$ = 24.0 ± 3.5 ms), and V2 achieved the highest signal-to-noise ratio (SNR) across all pulse trains (SNR to 20AP V2: 115.1 ± 25.6, V2.6: 62.8± 6.6, V2.7b: 23.2± 4.8) (**Figures 2A and S2C, Table S2**).

With JF585, V2.7b was able to better resolve individual pulses of repeated pulse trains due to its fast decay (V2: $t_{1/2}$= 731 ± 29.9 ms, V2.6: $t_{1/2}$ = 97.4 ± 3.2 ms, V2.7b: $t_{1/2}$ = 20.4 ± 1.7 ms), while V2 and V2.6 exhibited higher peak $\Delta F/F_0$ and SNRs across trains (**Figures 2B and S2C-E**). With JF646, V2.6 exhibited substantially larger $\Delta F/F_0$ and higher SNR than V2 (**Figures 2C and S2C-E**), though both sensors showed slower decay kinetics than with JF585 or JF635. (SNR to 20AP V2: 35.8 ± 3.4, V2.6:107.9 ± 29.8; $t_{1/2}$ to 1AP V2: 861± 137 ms, V2.6: 638 ± 54.5 ms) (**Figure S2E**).

We characterized V2 and V2.6, the highest-SNR variants in neuronal culture, using two-photon (2P) imaging of electrically evoked glutamate release in acute brain slices across several brain regions. We first obtained 2P excitation spectra of the sensors stably expressed in HEK293T cells and labeled with JF585 and JF635, revealing consistency with previous 2P characterization[19] of HaloTag-dye conjugates (iHaloGluSnFR-JF635 peaks at 790 nm and ~1200nm, and iHaloGluSnFR-JF585 at 820 nm and 1120 nm; **Figure S2F**). We injected AAV encoding iHaloGluSnFR-V2.6 driven by the synapsin promoter (AAV1-hSyn:iHaloGluSnFR-V2.6) in cortex (M1), hippocampus (HPC), and dorsolateral striatum (DLS). After 5 weeks of expression, we cut brain slices, incubated them with JF635, and performed 2P imaging with 1200 nm excitation and electrical stimulation (**Figure 2D**). V2.6 labeled with JF635 showed fast, stimulus-scaled responses in all regions, and resolved single-pulse (1P) events in M1 and DLS (5P cortex: $\Delta F/F_0$ =107.4 ± 33.9%, $t_{1/2}$=41.7 ± 13.0 ms; DLS: $\Delta F/F_0$ =54.6 ± 18.1%, $t_{1/2}$=36.5 ± 14.3 ms; HPC: $\Delta F/F_0$ =29.6 ± 16.0%, $t_{1/2}$=36.0 ± 13.6 ms; **Figure 2E-H and Table S3**). We compared the performance of V2.6 with V2 in acute HPC and DLS slices. V2.6 yielded higher peak $\Delta F/F_0$ in DLS and significantly faster kinetics compared to V2, whereas V2 yielded higher peak $\Delta F/F_0$ in HPC (5P V2 HPC: $\Delta F/F_0$ =54.3 ± 23.1%, $t_{1/2}$= 456.4 ± 73.8 ms; DLS: $\Delta F/F_0$ =29.0 ± 13.5%, $t_{1/2}$= 388.5 ± 117.0 ms; **Figures 2I and S2G**). V2.6 with JF585, excited at 1100 nm, yielded similarly robust responses (5P $\Delta F/F_0$ =86.7 ± 60.6%, $t_{1/2}$=80.5 ± 5.8 ms, **Figures 2J and S2H**), providing a blue-shifted option for multiplexed imaging.

Together, iHaloGluSnFR provides a modular chemigenetic platform supporting the use of bright red and far-red JF dyes, consisting of high-affinity (V2) and high–dynamic-range (V2.6, V2.7b) variants that can detect single-pulse glutamate release with tunable affinity, kinetics, and spectra, and are compatible with 2P imaging in diverse brain regions.

Quantal imaging of heterogeneous glutamate release at synapses with iHaloGluSnFR

Glutamate transmission is essential for synaptic computation. We therefore tested whether iHaloGluSnFR could detect glutamate release at individual synapses. We first characterized the ability of iHaloGluSnFR to detect “optical minis”: nonsynchronous, synaptic glutamate release triggered by hyperosmotic sucrose in TTX-silenced neurons[6,7] (**Figure S3A-D**). Sensors that displayed fast kinetics in field stimulation experiments (V2.6-JF635, V2.6-JF585, V2.7b-JF585) produced robust, high SNR, fluorescent transients with release site densities and kinetics comparable to those seen with iGluSnFR3(v857)-GPI, and asynchrony that is consistent with what is expected of osmotic shock dependent spontaneous release (**Figure S3A-D**).

We next evaluated the sensitivity of iHaloGluSnFR-V2.6 at single synapses. We used mouse hippocampal cultures sparsely transfected with iHaloGluSnFR-V2.6 incubated with JF585 dye. We performed whole-cell patch-clamp recording in putative pyramidal neurons expressing the sensor and stimulated with 50-pulse 5Hz trains (**Figure 3A**). A region containing a dense presynaptic axonal arbor of the patched neuron was selected for imaging, where we found that iHaloGluSnFR captured release at multiple boutons in the axonal arbor of the same neuron (**Figure 3B-C**).

We next asked whether iHaloGluSnFR-V2.6 enables estimation of quantal glutamate release parameters[23–30]. Quantal analysis of deconvolved fluorescent traces permitted the estimation of release probability (Pr) for each bouton, and illustrated substantial heterogeneity of release rates between boutons (**Figures 3D-F and S3E-G**). Additionally, by using a 20 Hz paired-pulse stimulation, we obtained the bouton-specific paired-pulse ratio (PPR), a key feature of short-term plasticity (**Figures 3D-E and S3E-G, Table S4**). Thus, iHaloGluSnFR possesses the kinetics and sensitivity to enable spatially constrained, quantal-resolution imaging of glutamate release at many individual synapses at a time, providing measures of relative basal synaptic weight (Pr) and short-term plasticity (PPR).

Multiplexed imaging of glutamate and calcium in individual synapses

Multiplexed imaging of glutamate release and intracellular calcium transients would provide a powerful approach for elucidating input–output transformations at synapses. To overcome the spectral limitations of GFP- and YFP-based glutamate sensors, we tested the utility of iHaloGluSnFR for dual-color imaging with genetically encoded calcium indicators.

We injected AAVs encoding GCaMP6s (hSyn-FLEX:axon-GCaMP6s) in CA3 and iHaloGluSnFR-V2.6 (hSyn: iHaloGluSnFRV2.6) in contralateral CA1 of DRD1-Cre mice (**Figure 4A**). Using dual-color two-photon imaging (GCaMP6s: 920 nm and V2.6-JF635: 1200 nm), we observed GCaMP-expressing axons projecting from CA3 intermingled with V2.6-expressing dendrites in CA1 when labeled with JF635 (**Figure 4A**). Electrical stimulation evoked simultaneous glutamate and presynaptic calcium in CA1 with distinct peak amplitudes (5p iHaloGluSnFR-V2.6: $\Delta F/F_0$=21.0 ± 15.1%, 5p GCaMP6s: $\Delta F/F_0$=8.5 ± 1.6%) and kinetics (5p iHaloGluSnFR-V2.6: $t_{1/2}$=41.4 ± 25.9 ms, 5p GCaMP6s: $t_{1/2}$=1.2 ± 0.65 s) (**Figure 4B-C**). To exclude potential fluorescence cross-talk between sensors, we incubated the slices with DL-*threo*-β-Benzyloxyaspartic acid (TBOA), a potent glutamate transporter (EAAT) inhibitor. TBOA selectively altered iHaloGluSnFR signals without affecting presynaptic calcium transients (**Figure 4B-C**). During 5 pulse stimulation, TBOA slowed the decay rates of iHaloGluSnFR responses (TBOA: $t_{1/2}$=671.7 ± 263.3 ms, P=0.013). Under 20 pulse stimulation, TBOA increased peak iHaloGluSnFR amplitudes (TBOA: $\Delta F/F_0$= 213.7 ± 118.5%, P=0.039) and further slowed fluorescence decay (TBOA: $t_{1/2}$= 760.2 ± 410.4 ms, P=0.038) (**Figure 4C**). In both conditions, TBOA produced no change in the peak amplitude or decay kinetics of presynaptic calcium signals (**Figure 4C**), confirming that the two sensors are spectrally independent.

We then examined the spatial and functional correlation between presynaptic calcium and glutamate release. iHaloGluSnFRV2.6 is expressed broadly in CA1 neurons, including in PSD-95 expressing dendritic processes which are closely opposed to GCaMP-positive boutons (**Figure 4D**). Calcium transients detected by GCaMP was largely restricted to CA3 axon boutons (**Figure 4E**). We observed broad glutamate responses across the field of view, with robust signals at sites overlapping GCaMP6s-positive boutons (**Figure 4E**). Quantification of bouton-centered responses revealed a positive correlation between presynaptic calcium and glutamate release at the same location (r = 0.26 at 0 μm), which declined with distance and was significantly reduced beyond 5 μm (r > 5 μm) (**Figures 4F and S4A-B**). This spatially coupled activity between presynaptic calcium and local glutamate suggests synaptic communication between the GCaMP-labelled projections with the iHaloGluSnFR-expressing CA1 cells.

To test whether red-shifted iHaloGluSnFR enables multiplexed neurochemical imaging with blue-shifted neuromodulator sensors, we co-expressed AAVs encoding iHaloGluSnFR-V2.6 (hSyn:iHaloGluSnFR-V2.6) and Cre-dependent AAV encoding dLight3.8 (hSyn-tTA-TRE-DIO:dLight3.8)[31] (**Figure S4C**). Dual-color two-photon imaging of DLS in acute slices simultaneously detected electrically evoked glutamate and dopamine release (**Figure S4C-D**). Pharmacological manipulations confirmed sensor specificity and spectral separation: TBOA and the dopamine reuptake blocker methylphenidate (MPD) selectively increased the peak amplitudes and slowed decay kinetics of iHaloGluSnFR-V2.6 and dLight3.8 fluorescence transients, respectively (V2.6-JF635 Vehicle 20P: $\Delta F/F_0$ =38.5 ± 12.3 %, $t_{1/2}$=58.0 ± 3.9 ms, TBOA: $\Delta F/F_0$ = 209.4 ± 60.0 %, $t_{1/2}$=658.5 ± 93.3 ms; dLight3.8 Vehicle 20P: $\Delta F/F_0$ =17.3 ± 18.0 %, $t_{1/2}$=94.6 ± 70.5 ms, TBOA+MPD 20P: $\Delta F/F_0$ =21.8 ± 17.5 %, $t_{1/2}$=4.0 ± 2.8 s) (**Figure S4D-E**).

Dual-color fiber photometry of glutamate and dopamine in operant reward learning

Dissecting how glutamate signals and neuromodulators act collectively to shape behavior requires simultaneous recording of multiple neurochemicals. After validating multiplexed detection in acute brain slice, we examined glutamate and dopamine dynamics in the ventral tegmental area (VTA) during operant reward learning. To utilize iHaloGluSnFR *in vivo*, we first determined methods to deliver the dyes *in vivo*. Although we successfully delivered JF646 both cortically and subcortically via intravenous and intrathecal delivery (**Figure S4F-H**), we opted to utilize JF635-bound sensor versions for their high dynamic range, tunable kinetics, and spectral separation from green sensors (**Figures S1E-H and S2D-E**). We broadly expressed iHaloGluSnFR-V2.6 or V2 with sparsely expressed dLight3.8 in the VTA of DRD1-Cre mice, and implanted an optofluidic implant for dye infusion and fiber photometry (**Figures 5A-B and S5A**). Five hours after JF635 dye infusion (to allow for dye capture and clearance of unbound dye), freely moving mice performed an operant reward paradigm that was initiated by a tone (**Figure 5C**). The animal turns off the tone by maintaining nose-poke at an action port, after which a water reward becomes available at the reward port. After poke-triggered reward delivery, a 10-20 second variable intertrial interval (ITI) commences, and a trial reinitiates with a new tone (**Figure 5C**). Expert animals (trained $\geq$7 sessions) exhibited ~9-fold faster reward collection times than novice animals (novice: 35.8 ± 15.4 s, expert: 3.9 ± 3.0 s, n=13 animals) (**Figure 5D**). Upon reward port pokes, we observed a sustained reduction in glutamate activity, whereas after transiently decreasing, dopamine signals increased (**Figures 5E and S5B-C**). Overall, glutamate and dopamine signals covaried where their maximum cross-correlation increased with learning (novice mean peak correlation=0.23 ± 0.14, expert mean peak correlation= 0.46 ± 0.20, *P*=0.011, two-sided paired t-test, n=13 animals) (**Figure 5F**). Across learning, the temporal lag between the two signals narrowed from ~150 ms to ~50 ms, with iHaloGluSnFR signals preceding dLight signals (**Figure 5F insets**).

To parse how these signals are modulated across learning, we compared glutamate and dopamine signals between expert and novice animals. To first determine if the reduction in glutamate is specific to reward consumption, we compared photometry signals between rewarded and unrewarded pokes. Both novice and expert animals displayed an overall reduction in glutamate for rewarded as compared with unrewarded pokes defined when animals erroneously poke the reward port during the tone (Glu novice: *P*=0.0006, expert: *P*=0.048, two-sided t-test, n=13 animals) (**Figures 5G and S5D**). In contrast, dopamine responses were similar between rewarded and unrewarded pokes in both novice and expert animals (DA novice: *P*=0.15, expert: *P*=0.65, two-sided t-test, n=13 animals) (**Figures 5G S5D**). It is worth noting that the faster, higher dynamic range V2.6 yielded a larger magnitude dip in response to reward consumption compared to iHaloGluSnFR-V2 (Novice V2.6: area under the curve (AUC)= -3.8 ± 2.4, V2: AUC= -1.1 ± 1.7) (**Figure S5D**), whereas the higher affinity V2 sensitively reported a reward-triggered transient rise in glutamate upon reward delivery before the sustained reduction seen in novice animals (**Figure S5D, arrows**).

Next, we compared action-triggered glutamate and dopamine transients immediately before reward collection in expert versus novice animals. Both signals exhibited sharper anticipatory peaks in experts compared to novices as the animals approached the reward port (glutamate: *P*= 0.0004; dopamine: *P*= 0.0016, paired t-test) (**Figures 5H and S5E**). This pre-reward increase in signal occurred ~1 s prior to entry into the reward port in expert animals, co-occurring with action port entry (**Figure 5H, dashed line**). In contrast, we did not observe significant changes in peak amplitudes following reward port entry comparing expert versus novice animals (glutamate: *P*=0.83; dopamine: *P*=0.42, paired t-test) (**Fig 5H**).

Motivated by distinct activity changes across task epochs, we reanalyzed the cross-correlation between dopamine and glutamate signals within each epoch. With learning, the correlation between glutamate and dopamine signals significantly increased only during reward approach (*P*= 0.0085, paired t-test), whereas correlation during reward consumption did not change (*P*= 0.34, paired t-test) (**Figure 5I**). In expert animals, the peak correlation of action-triggered glutamate–dopamine transients exceeded that of the reward-triggered correlation (*P* = 0.0075, paired t-test), a difference not observed in novices (*P* = 0.48, paired t-test) (**Figure 5I**). We further performed single-trial regression analysis which revealed that action-triggered glutamate signaling predicts reward port entry, confirming its role in encoding motivated approach (**Figure S5F-G**).

As a control, we recorded from a separate cohort of wild-type animals expressing the established green fluorescent SF-iGluSnFR-A184S in the VTA (**Figure S5H-I**). In both novice and expert animals, iGluSnFR signals showed a ramp in signal preceding reward collection and a decrease after reward delivery that was reward specific (novice: *P* = 0.018; expert: *P* = 0.021, paired t-test; n = 6 animals) (**Figure S5J-L**). Although reward-aligned iGluSnFR signals in expert animals showed a trend toward a small anticipatory increase in signal, this was not significant (*P* = 0.53, paired t-test, **Figure S5M**), highlighting that the sensitivity of iHaloGluSnFR allowed reliable detection of this learning-dependent change compared with iGluSnFR.

Together, these findings demonstrate that the red-shift and high sensitivity of iHaloGluSnFR enable simultaneous, task-specific measurement of glutamate and dopamine transients, revealing correlated yet dissociable functions. Glutamate exhibited a biphasic response, rising with reward approach and decreasing during reward consumption, while dopamine closely tracked the reward approach. With learning, glutamate and dopamine signals become more tightly coupled during the motivated approach but remain distinct during reward consumption.

DISCUSSION

iHaloGluSnFR is a versatile platform with red-shifted spectral flexibility for imaging glutamate in multiplex with blue-green reporters. We present 9 sensors in the iHaloGluSnFR family-- three versions of the protein sensor bound to one of three fluorogenic JF dyes (**Figure 1**), yielding sensors with differing dynamic range, affinity and kinetics, suitable for a wide range of applications. The sensitivity and kinetics of the sensors *in vitro* are comparable to the most advanced glutamate sensors available [6,7], with high SNR detection of single action potential evoked transmitter release events and fast kinetics (**Figure 2**). The ability to combine each scaffold with several Janelia Fluor dyes that we tested suggests that it will be possible to further extend spectral variety with other dyes.

We show that iHaloGluSnFR can detect spontaneous (“optical minis”) and stimulus-evoked transmitter release with quantal resolution, making it possible to perform optical analysis at dozens of synapses simultaneously to derive synaptic weights and measure short-term plasticity. Our measurements in individual hippocampal pyramidal neurons in culture illustrate remarkable heterogeneity in glutamate release properties between synapses in a single axonal arbor (**Figure 3**), which has only been previously characterized with calcium or GFP-based glutamate indicators [23,26–28,30,32–34]. iHaloGluSnFR could be coexpressed with spectrally distinct calcium or neuromodulator sensors in different cells within a circuit for multiplexed imaging. In combination with GCaMP6s, we could relate presynaptic calcium to glutamate release at individual presynaptic boutons (**Figure 4**). Weak correlation between these signals is consistent with the known contribution to bulk presynaptic calcium of influx through both Ca_v channels that are localized to the active zone, which couple to release, and those that are located elsewhere in the bouton, too far to trigger release.

We demonstrate that iHaloGluSnFR is capable of simultaneous, task-specific measurement of glutamate and dopamine transients *in vivo*. In combination with our newest dopamine sensor, dLight3.8, we measured glutamate and dopamine in the VTA during learning in an operant foraging task (**Figure 5**). The VTA contains heterogeneous cell types receiving diverse glutamatergic inputs [35], yet how glutamate shapes local neuromodulator release during reward learning remains unclear. Using dual-color fiber photometry with iHaloGluSnFR and dLight3.8, we found that VTA glutamate integrates motivational drive and reward outcome and becomes progressively more correlated with dopamine as animals learn the task. Glutamate consistently preceded dopamine and its latency shortened with learning (**Figure 5F**), suggesting that glutamate drives dopamine release specifically during reward-predictive actions rather than during consumption. This strengthening of glutamate–dopamine correlation was task-specific and was enhanced during motivated action, but not at reward consumption, indicating that learning selectively enhances glutamate-dopamine interaction to encode reward expectation rather than received reward (**Figure 5I**). While glutamatergic inputs to VTA have been shown to reinforce and encode prediction[36–38], iHaloGluSnFR reveals a biphasic glutamate pattern: a brief anticipatory peak before reward, followed by a sustained decrease during consumption, consistent with disinhibition-mediated suppression of dopamine[39,40]. Thus, we have shown that VTA glutamate is not merely a “reward signal,” but also a dynamic integrator of motivation and expectation that, with learning, becomes a temporal driver of dopamine signaling.

Limitations of the study

iHaloGluSnFR expands a growing class of chemigenetic biosensors that are orthogonal to highly-optimized fluorescent protein-based biosensors. While synthetic calcium and voltage dyes have historically been used for real-time imaging of neural activity[41–45], their lack of cell-type specificity limits circuit-level application. Chemigenetic sensors address this gap by combining genetically encoded targeting with the favorable photophysical properties of small-molecule dyes. However, a principal limitation of the chemigenetic approach is the limited bioavailability of some dyes when delivered exogenously to the brain[46]. We solved this challenge by establishing a dye delivery method compatible with chronic *in vivo* recording, leveraging the low unbound fluorescence of fluorogenic Janelia Fluor dyes and time-dependent clearance of excess dye[19]. Despite this advance, broader applications of chemigenetic tools such as iHaloGluSnFR will require further optimization of less-invasive and more scalable implantable delivery platforms. Such improvements would expand the range of usable dyes and make repeated or long-term labeling more practical. Although we successfully delivered JF646 systemically for sensor labeling, many dyes with favorable photophysical properties remain impractical due to limited brain bioavailability. Future dye-delivery strategies, potentially informed by advances in small-molecule drug delivery, such as nanoparticles, would significantly broaden the use of chemigenetic sensors for *in vivo* recording. In parallel, photo-induced electron transfer–based reporters using far-red and near-infrared non-fluorogenic dyes with improved bioavailability and fluorescence lifetime modulation have recently been developed[16]. While these chemistries are not currently compatible with iHaloGluSnFR, continued protein engineering efforts may enable their incorporation into next-generation sensors. More broadly, the dye-delivery framework described here provides a generalizable approach for broadening *in vivo* applications of chemigenetic sensors that rely on dyes with limited bioavailability, including those for calcium, voltage, dopamine, and reactive oxygen species[18,47,48].

RESOURCE AVAILABILITY

Lead contact

Further information and requests for resources and reagents should be directed and will be fulfilled by lead contact, Lin Tian, lin.tian@mpfi.org

Materials availability

The following plasmids, deposited in Addgene, will be made available at the time of publication: pAAV-hSyn-iHaloGluSnFR-V2-GPI (252666), pAAV-hSyn-iHaloGluSnFR-V2.6-GPI (252668), pAAV-hSyn-iHaloGluSnFR-V2.7b-GPI (252669).

Data and code availability

- All source data and original code has been deposited at Figshare: https://Figshare.com/s/22a5dfa9a8cf5aca0932
- Any additional information is available from the lead contact upon request.

ACKNOWLEDGEMENTS

We thank Dr. Jiandi Wan and Brianna Urbina (UC Davis) for providing imaging support. We also thank Shimon Yudovich for their help setting up the optics for quantal analysis experiments, Jacob Roshgadol for designing the behavioral paradigm and engineering the device, and Dr. Emily Wright for aiding in dye delivery experiments. We also thank Lisa Nguyen for imaging histology samples, and Brenda Garcia, Julia Sutedjo, and Katelyn Ramsahai for their assistance in cloning and plasmid preparation. We thank Leomara H. Swanson (University of Pennsylvania) for their assistance in histology in the systemic dye delivery study. We thank Dr. Lesley Colgan for her assistance with the figures and Dr. Jenny Yu at the MPFI molecular core. We thank Dr. Kiyoto Kurima and Dr. Jeff Wickens (OIST) for providing dLight viruses. This work was supported by the Keck Foundation (L.T.), National Eye Institute (R21EY031858 to L.T.), National Institute of Neurological Disorders and Stroke (F31NS129379 to N.T., U01NS120820 to L.T., R01NS107506 to E.Y.I., R01NS140454 to G.C. and L.T.), National Institute of General Medical Sciences (T32GM099608, funding N.T.), National Institute of Mental Health

(UM1MH136462 to L.T.), National Institute on Drug Abuse (F31DA062445, to C.S.O.), and Chan Zuckerberg Initiative (2024-351072 to E.Y.I.). E.R.S. and L.D.L. are supported by the Howard Hughes Medical Institute (HHMI).

AUTHOR CONTRIBUTIONS

L.T. and E.Y.I supervised the project. L.T. and A.A. conceptualized the project. N.T. engineered and characterized the sensors. P.R.F.M. performed quantal analysis experiments under the supervision of E.Y.I. J.Y.M. and N.T. performed fiber photometry experiments. J.A.C. performed 2-photon acute slice experiments and characterization with support from N.T. J.A.C., Y.J., and J.Y.M. performed all mouse surgeries. N.T. performed data analysis for 2-photon and fiber photometry experiments. C.S.O., and G.C. performed systemic dye delivery experiments and histology. D.O. and H.I. aided in fiber photometry analysis. L.D.L. provided all dyes used, and L.D.L. and E.R.S. aided in directing the chemigenetic strategy. N.T. and L.T. wrote the original draft, with input and edits from all other authors.

DECLARATION OF INTERESTS

L.D.L is a scientific cofounder, shareholder, and consultant of Eikon Therapeutics. US Patent 9,933,417 describing azetidine-containing fluorophores and variant compositions (with inventor L.D.L) is assigned to HHMI.

SUPPLEMENTAL INFORMATION

Document S1: Tables S1-S4, Data S1

MAIN TEXT FIGURE TITLES AND LEGENDS

Figure 1. iHaloGluSnFR development and characterization in vitro.

(**A**) Schematic of iHaloGluSnFR mechanism. (**B**) Simulated structure of iHaloGluSnFR-V2 bound to JF635 HaloTag ligand with key mutations highlighted in green. (**C**) Schematic of the gene encoding the sensor with mutations acquired for the three key versions of iHaloGluSnFR. (**D, E, F**) *In situ* glutamate titration of sensor-expressing stable HEK293T cell lines fit to the Hill equation for key variants bound to JF635 (**D**), JF585 (**E**), or JF646 (**F**) dye-ligands. Insets are representative images of cells expressing the sensor at saturation and their corresponding ∆F/F heatmaps (n=3-6 cultures for each dye/sensor/concentration combination). (**G, H, I**) Per-molecule brightness with and without 200 µM glutamate of stably expressing HEK293T expressing iHaloGluSnFR-TS-Citrine bound to JF635 (**G**), JF585 (**H**), or JF646 (**I**). (G) JF635 group-wise apo: *P=0.017, Glu: *P=0.023. (H) JF585 group-wise apo: *P=0.024, Glu: P=0.37. (I) JF646 group-wise apo: **P=0.0073, Glu: P=0.146 (n=4 for each condition). Data are plotted as mean ± SD. P-values determined by Kruskal-Wallis across variants.

Figure 2. iHaloGluSnFR characterization in dissociated neuronal culture and two-photon imaging of acute brain slices

(**A**) Whole field stimulation responses to 1 action potential (AP) and its decay $t_{1/2}$ (shown as mean ± SD) for iHaloGluSnFR versions with JF635 (inset shows V2.6 and V2.7b $t_{1/2}$). Group-wise ***P =2.02E-07 (top). Responses to 5, 10, 20 AP 30Hz 4V field stimulation (middle) and peak signal-to-noise ratio (SNR) of variants with JF635 (bottom). Group-wise in order of pulse number for SNRs: *P =0.01, ***P =0.0003, ***P=9.4E-05, ***P=7.0E-05 (bottom, n=5-7 cultures and 9-17 field of views (FOVs) per sensor version). (**B**) Field stimulation characterization of iHaloGluSnFR-expressing neurons incubated with JF585. 1 AP responses, 1 AP decay $t_{1/2}$ (top, shown as mean ± SD, group-wise ***P=1.8E-05), and responses to AP trains (middle) and peak SNR (bottom). Group-wise in order of pulse number for SNRs: P =0.39, P =0.76, P =0.09, P =0.06 (bottom) (n=3 cultures and 6-10 FOVs per sensor version). (**C**) iHaloGluSnFR-JF646 1AP responses and decay $t_{1/2}$ (shown as mean ± SD, P=0.32) (top), responses to AP trains (middle), and peak SNR (bottom). Group-wise in order of pulse number for SNRs: P=0.15, P=0.08, *P=0.03, *P=0.02 (bottom) (n=3-4 cultures and 6-7 FOVs per version). (**D**) Schematic of acute slice simultaneous 2p imaging and electrical stimulation. (**E, F, G**) V2.6-JF635 responses expressed in M1 (**E**), DLS (**F**), and HPC (**G**) in acute slice imaged under 2-photon excitation and stimulated with 40 Hz pulse trains (0.2 ms pulse width, 10V). Shown as mean ± SEM (n=3-4 animals per brain region). (**H**) Quantification of E-G fluorescence decay kinetics (top) and peak $\Delta F/F_0$ (bottom). Shown as mean ± SD. (**I**) Comparison of peak $\Delta F/F_0$ (left) and decay $t_{1/2}$ (right) of V2-JF635 and V2.6-JF635 in striatum (DLS) and hippocampus (HPC) (n=3-4 animals per sensor/brain region). Shown as mean ± SD. (**J**) Comparison of peak $\Delta F/F_0$ (left) and decay $t_{1/2}$ (right) of V2.6-JF585 with V2.6-JF635 signals from hippocampus stimulation. Shown as mean ± SD (n=3-4 animals per dye-sensor combination). The same V2.6-JF635 quantification data shown in H are also shown in I-J to compare different dye-sensor combinations. Unless otherwise noted, all dissociated neuronal culture whole field stimulation data are shown as mean ± SEM, with Kruskal-Wallis tests followed by Dunn's post-hoc tests (Holm correction). All acute slice statistical tests are Wilcoxon rank-sum tests (Holm correction). N.S., not significant *P* >0.05, * *P* <0.05, ** *P* <0.01, *** *P* <0.001.

Figure 3. iHaloGluSnFR can detect presynaptic bouton activity and monitor quantal synaptic responses.

(**A**) Cultured mouse hippocampal neuron expressing iHaloGluSnFR V2.6 labelled with JF585, where a region of interest with a dense axonal arbor was selected for imaging in voltage-clamp mode at 5 Hz x 50 action potentials. Scale bar: 50 µm. (**B**) Maximum projection image of the Gaussian bandpass-filtered image stack (0.2 Hz - 20 Hz), revealing all active presynaptic boutons during the 5 Hz stimulation train. Scale bar: 20 µm. (**C**) V2.6-JF585 responses from selected boutons within the ROI, revealing the heterogeneous activity of synapses supplied by the same axon. (**D-E**) Quantal analysis for 2 boutons highlighted in B and C. Raw traces were deconvolved using a single quantum waveform (top). A histogram of peak amplitudes from those that exceed 4 SD from the baseline were fit to a multi-gaussian distribution (right plot) to distinguish single and multi-quantal events (dashed line indicates 4 SD, continuous green line on deconvolved trace indicates quantal amplitude). From responses to 20 Hz paired pulse stimulation, optical paired pulse ratios were determined (bottom). (**F**) Release properties across all boutons (n=120 boutons). Mean ± SEM release for each pulse in the 5 Hz stimulus train (left), and distribution of average release rate at steady state (>5th AP, right).

Figure 4. iHaloGluSnFR can be used for multiplexed imaging with calcium and neuromodulator sensors in acute slice.

(**A**) Sensor injection strategy of AAV-hSyn:iHaloGluSnFR-V2.6 in CA1 and AAV-hSyn-FLEX:axon-GCaMP6s in contralateral CA3 in DRD1-Cre animals. Example histological slice image demonstrating expression: magenta V2.6-JF635, green GCaMP6s, blue Hoechst nuclear stain (middle). Scale bar: 1mm. Representative 2P average projection image during electrical stimulation: magenta V2.6-JF635, green GCaMP6s (bottom). Scale bar: 50 µm. (**B**) Mean ± SEM fluorescence responses to 5 pulse (5p) and 20 pulse (20p) stimulation trains, treated with vehicle (DMSO) or 200 nM TBOA (n=3 animals, 4 slices). (**C**) Quantification of peak $\Delta F/F_0$ and decay $t_{1/2}$ of traces from (B) with and without 200 nM

TBOA. Shown as mean ± SD (Shapiro-Wilk test P>0.05, followed by two-sided paired t-tests). (**D**) Representative histology image (top) of colocalization of PSD95 (cyan) with V2.6-JF585 (magenta) and contact with GCaMP6s (green). Scale bar: 50 μm. 3D reconstruction of dashed boxed region with PSD95 puncta (cyan dots), with boxed regions highlighting regions of contact between PSD95 and GCaMP (bottom). Scale bar: 5 μm. (**E**) Example field of view of V2.6-JF585 (magenta) and GCaMP6s (green) signals (top left), with corresponding $\Delta F/F_0$ heatmaps of V2.6-JF585 (top middle) and GCaMP6s (top right). Scale bar: 5 μm. Fluorescence responses to 10 pulse electrical stimulation of labeled boutons for GCaMP and overlapping iHaloGluSnFR signal (mean ± SEM, n=3 animals). (**F**) Significance heatmap of the Pearson's correlation between peak iHaloGluSnFR and GCaMP signals in response to 5 pulse electrical stimulation at all boutons in the representative FOV shown in E, where iHaloGluSnFR signal is analyzed at different distances radiating away from the bouton. Greater -log(*P*) (more saturated magenta) indicates greater significance of the Pearson's correlation between iHaloGluSnFR and GCaMP (n=110 boutons).

Figure 5. iHaloGluSnFR and dLight3.8 fiber photometry in VTA during operant reward behavior. (**A**) Schematic of virus injection (AAV-hSyn-tTA-TRE-DIO:dLight3.8 and AAV-hSyn:iHaloGluSnFR-V2.6 or V2) and dye infusion strategy for dual color recording using an optofluidic implant to infuse dye 5-6 hours before recording in DRD1-Cre mice. (**B**) Example histological slice images of recording site and sensor expression of dual color animals (magenta signal from iHaloGluSnFR-V2.6-JF635 and green from dLight3.8). Scale bars: 500 μm (top), 200 μm (bottom). (**C**) Operant reward behavior paradigm during which fiber photometry is recorded, where mice are trained to nosepoke at an action port when a tone plays, which subsequently turns off the tone and makes a water reward available at the reward port. (**D**) Experts (trained $\geq$7 sessions) take less time to collect reward from the start of the trial than novices (recorded during their 1st or 2nd session). Shown as mean time to reward ± SD. ****P*=2.2E-5 (n=13 animals). (**E**) Expert animals' single trial z-scored iHaloGluSnFR-V2.6 (left) and dLight3.8 (right) photometry signals aligned around reward dispense at t=0 (n=6 animals). (**F**) Cross-correlation between trial-chunked iHaloGluSnFR-V2 or V2.6 (pooled) signals with dLight3.8 signals within animal across time lags, where the iHaloGluSnFR signal is shifted by the indicated time lag with respect to dLight (left). The peaks of the average cross-correlation trace for novice animals occur at -150 ms, and expert animals at -50 ms time lags (insets), where iHaloGluSnFR leads dLight. Grey curves are shuffled controls. Shown as mean ± SEM. Mean ± SD peak cross-correlation across all time lags of either expert or novice animals (right). **P*=0.011 (n=13 animals). (**G**) (Top) Average z-score ± SEM of photometry signals aligned to either rewarded pokes or unrewarded pokes (futile reward port pokes when the tone is on) at t=0, and (bottom) mean ± SD area-under-the-curve (AUC) 0 to 5 seconds after

the reward port poke in novice trials (left) and expert trials (right) for iHaloGluSnFR (pooled V2 and V2.6) and dLight. Novice: Glu ****P*=0.0006, DA *P* =0.15; Expert: Glu **P*=0.0483, DA *P*=0.65 (n=13 animals, 1202 expert trials, 350 novice trials). (**H**) Mean z-score ± SEM glutamate and dopamine photometry signals aligned to rewarded pokes (at t=0) across learning (left). The dotted vertical line indicates the mean latency to poke the action port before reward collection in expert trials. Maximum increases in signal before (shaded beige) and after reward delivery for iHaloGluSnFR and dLight across learning, shown as mean ± SD (right). Glu pre-reward: ****P*=0.0004, post-reward: N.S. *P*=0.828; DA pre-reward: ***P*=0.0016, post-reward: N.S. *P*=0.42 (n=13 animals). (**I**) Mean ± SEM cross correlation of dopamine and glutamate z-scored signals pre-reward dispense (-2 to 0 seconds) and post-reward dispense (0 to 2 seconds) at different lag times, where glutamate is shifted with respect to dopamine (left). Mean ± SD peak correlation for pre- and post-reward delivery, comparing novice and expert signals (right). Pre-reward novice vs. expert ***P*=0.00847, post-reward novice vs. expert N.S. *P*=0.335; pre and post-reward signals novice N.S. *P*=0.479, expert ***P*=0.0075 (n=13 animals). Shapiro-Wilk tests were performed before paired two-sided t-tests. N.S., not significant *P* >0.05, * *P* <0.05, ** *P* <0.01, *** *P* <0.001.

SUPPLEMENTAL FIGURE TITLES AND LEGENDS

Figure S1: iHaloGluSnFR engineering and *in situ* characterization

(**A**) Representative image of transfected HEK293T expressing V0, bound to JF635, before and after 5 mM glutamate addition (top). Time course of 5 mM glutamate addition in 3 cultures (bottom, individual replicates are in grey, the mean response is in black). Scale bar: 20 µm. (**B**) Comparison of mutations introduced to key variants in iHaloGluSnFR development, where underlined positions are those screened to generate the next intermediate variant, and magenta residues indicate a new mutation introduced. Initial linker screening and targeted mutations to modulate the glutamate affinity evolved the prototype construct (V0) expressed with the PDGFR transmembrane domain to V2. Then, the PDGFR was switched out for Cobl9-GPI and underwent further screening at interface and linker positions to yield V2.6 and V2.7. (**C**) Dose-response curves of PDGFR-displayed intermediate versions of the sensor in transfected HEK293T cells. (n=1-4 cultures per concentration/variant). (**D**) Interface positions (red) tested based on the simulated structure of iHaloGluSnFR-V2, based on putative interactions with the dye (magenta, JF635) or dye-binding pocket. (**E**) Excitation and emission spectra of stably expressing HEK293T cells incubated with JF dyes with and without 100 µM glutamate. (n=3-6 per dye-sensor combination). (**F, G, H**) Comparison of glutamate response curves across different dyes for iHaloGluSnFR V2 GPI (F), V2.6 GPI (G), or V2.7b GPI (H) in stably expressing HEK293T (n=3-6 per condition, replotted data from Figure 1D-F). (**I**) *In situ* response of V2.6-JF635 in stably expressing HEK293T to 1 mM glutamate, GABA, dopamine, serotonin, histamine, and acetylcholine, and 1.6 mM of norepinephrine (****P*=6.8E-4, Wilcoxon rank-sum test of response to glutamate compared to all other neurotransmitters, n=3-4 for each ligand). Response to 50 µM CNQX, (R)-CPP, and TBOA. (***P*=0.004, Wilcoxon rank-sum test of response to glutamate compared to glutamatergic drugs). Inset is an expanded view of responses to off-target ligands. (**J**) Dose-response curves of V2.6-JF635 in stably expressing HEK293T cells with varying concentrations of aspartate (EC50= 43.4 ± 26.5 µM) compared to its responses to glutamate (EC50=12.4 ± 3.3 µM) (n=4 for aspartate, n=4-6 for glutamate). N.S., not significant *P* >0.05, * *P* <0.05, ** *P* <0.01, *** *P* <0.001.

Figure S2: iHaloGluSnFR dissociated neuronal culture, acute slice, and 2-photon characterization

(**A-B**) Response of AAV-transduced E18 hippocampal neurons (AAV-hSyn:iHaloGluSnFR) expressing iHaloGluSnFR incubated with JF635 (A) or JF585 (B) to different concentrations of glutamate (left). Representative neurons and ∆F/F heatmaps of sensor-expressing neurons before and after addition of 1mM glutamate (right, at least n=3 cultures for each condition). Scale bars: 20 µm. (**C**) Peak ∆F/F in response to 4V 30 Hz whole field stimulation trains for iHaloGluSnFR sensor versions expressed in transduced neurons bound to JF635 (left, 5-7 cultures per version, group-wise in order of pulse number: **P*=0.02, *** *P*=0.00096, *** *P*=0.0006, *** *P*=0.0003), JF585 (middle, 3 cultures per version, group-wise in order of pulse number: *P* =0.28, *P* =0.26, *P* =0.096, *P* =0.06), and JF646 (right, 3-4 cultures per version, group-wise in order of pulse number: * *P*=0.046, * *P*=0.015, ** *P*=0.007, ** *P*=0.007). (**D**) Comparison of 1 AP and 20 AP responses across dyes and sensor versions (replotted data from Figure 2A-C, n=3-7 cultures per dye-sensor combination). (**E**) Quantification of 1 AP decay $t_{1/2}$ for each sensor version across dyes (left, group-wise V2: *P* =0.47, V2.6: *** *P*=1.5E-05, V2.7b: *P* =0.41, data replotted from Figure 2A-C). Peak ΔF/F across dyes for each sensor version (right, data also depicted in Figure S2C). (**F**) Two-photon spectrum of iHalo-V2.6 stably expressing HEK293T cells incubated with JF635 or JF585 dye-ligand. Plotted as mean ± SD (n=3-4 cultures per sensor). (**G**) ΔF/F traces of iHaloGluSnFR V2-JF635 expressed in hippocampus (HPC) (left) or dorsolateral striatum (DLS) (right) with 40 Hz electrical stimulation at t=0 (N=3-4 animals per brain region). (**H**) ΔF/F traces of iHaloGluSnFR V2.6-JF585 expressed in hippocampus (HPC) with 40 Hz electrical stimulation at t=0 (N=3 animals). All traces plotted as mean ± SEM. All statistical tests are Kruskal-Wallis tests with Dunn's post-hoc tests (Holm correction), N.S. not significant *P*>0.05, **P*<0.05, ***P*<0.01, ****P*<0.001.

Figure S3: iHaloGluSnFR permits synaptic imaging in dissociated neuronal culture

(**A**) Average projection image of iHaloGluSnFR V2.7b-expressing neurons (AAV1-hSyn:iHaloGluSnFR) incubated with JF585 treated with 1 µm TTX and 100 mM sucrose (top). Maximum projection image after temporal downsampling and subtracting baseline F_0 (middle). Detected release sites and release site density, quantified by number of detected release sites per mm^2 for different variants of iHaloGluSnFR and iGluSnFR3 (AAV1-CAG:iGluSnFR3-GPI-v857) shown as mean ± SD (bottom). Group-wise *P*=0.432. Scale bar: 20 µm. (**B**) Example traces from 16 unique release sites from (A) after 100 mM sucrose addition. (**C**) Comparison of peak ΔF/F (group-wise ****P*=1.6E-225) and (**D**) fluorescence decay rates (group-wise ****P*=3.3E-60) of optical minis across sensors. Kruskall-Wallis followed by Dunn's post-hoc (Holm correction) (n=3 cultures for iGlu3, V2.6-JF585, and V2.7b-JF585, and n=5 cultures for V2.6-JF635). N.S. not significant *P*>0.05, **P*<0.05, ***P*<0.01, ****P*<0.001. (**E**) Maximum projection image of glutamate release in boutons of a V2.6-JF585-expressing cell (as shown in Figure 3) after 50 action potentials stimulation at 5Hz, with 2 analyzed boutons highlighted. Scale bar: 20 µm (**F, G**) Voltage-clamp 5Hz 50 AP fluorescence response traces and deconvolved trace. Dashed line shows 4 SD from the baseline threshold for events to fit to a multi-gaussian function (right), and the single quantal threshold (green line) is derived from this fit. Lower plot depicts paired-pulse fluorescence response and the deconvolved trace. Quantal content, release rate, and paired-pulse ratio was derived for Bouton 12 (F) and Bouton 25 (G).

Figure S4: 2-color 2-photon acute slice and systemic dye delivery

(**A**) Method for bouton correlation peak analysis. The ΔF/F map of the downsampled axon-GCaMP6s image stack was used to identify active boutons. For each bouton, ring ROIs with widths of 5 pixels (0.594 um) were generated radiating out from the initial bouton ROI to quantify iHaloGluSnFR signal, where a dilation of 0 indicates the original bouton mask. The Pearson's correlation between iHaloGluSnFR and GCaMP peak ΔF/F of the downsampled image stacks across all boutons (110 boutons) for each ring dilation was determined. (**B**) Results for peak signal correlation analysis between iHaloGluSnFR and GCaMP with correlations plotted for dilated ring masks used for quantification. Middle plot shows the negative log of the p-value of the correlation, and the right plot shows the Pearson's correlation coefficient estimate for each ring dilation (data also shown in Figure 4F). (**C**) Injection scheme of AAV-hSyn:iHaloGluSnFR-V2.6 and AAV-hSyn-tTA-TRE-DIO:dLight3.8 in dorsolateral striatum (top). Representative average images before and during 20 pulse 40 Hz stimulation in acute slice (bottom). Scale bar: 20μm. (**D**) Representative fluorescence traces of responses to 20 pulse stimulation during treatment with Vehicle (DMSO), 200 nM TBOA, and 200 nM TBOA with 30 μM MPD. Shown as mean ± SD (n=3). (**E**) Quantification of peak $\Delta F/F_0$ and decay $t_{1/2}$ of V2.6-JF635 and dLight3.8 with pharmacological treatment under 20 pulse stimulation. Mean ± SD (n=2 animals, 3 slices). (**F**) Schematic and timeline for tests of retroorbital and intrathecal *in vivo* delivery of JF646. (**G**) Coronal slices of anterior cingulate cortex (ACC) and periaqueductal gray (PAG) with retroorbital (top) or intrathecal (bottom) dye delivery. (**H**) Cells labeled by dye (JF646, top), transduced with AAV1-hSyn-iHaloGluSnFR-V2.6 (anti-Myc tag, middle), and overlaid with retroorbital dye administration in PAG. Shapiro-Wilk test (P>0.05), followed by paired two-sided t-tests; N.S., not significant *P* >0.05, * *P* <0.05, ** *P* <0.01, *** *P* <0.001.

Figure S5: iHaloGluSnFR, dLight3.8, and iGluSnFR fiber photometry in VTA during operant reward behavior.

(**A**) Representative histology of dLight3.8 (green) and iHalo-V2-JF635 (magenta), counterstained with Hoechst (blue). Scale bar: 1mm. (**B**) Photometry signals for all iHaloGluSnFR-V2/dLight3.8 expert trials aligned around reward delivery (t=0) (n=7 animals). (**C**) Example novice animal's single trial glutamate (top) and dopamine (bottom) responses around reward dispense (t=0). (**D**) iHaloGluSnFR z-scored fluorescent traces aligned to reward port pokes either resulting in reward dispense or no reward (poke during the tone). Lower panel shows mean area-under-the-curve (AUC) post reward port poke. In Figure 5G, the data from both V2 and V2.6 shown here are pooled. Arrows indicate post-reward transient glutamate peaks. Novice V2: **P* =0.047, V2.6: ***P*=0.0042; Expert V2: *P* =0.92, V2.6: **P*

=0.015 (iHalo-V2: n=7, iHalo-V2.6: n=6 animals). (**E**) Example smoothed trace (black) overlaid on raw signal (grey) with extrema (red and blue) used to calculate peak increase of signal. (**F-G**) Mean AUC of receiver operating characteristic (ROC) of logistic regression models where binned glutamate z-scored signal (x-axis) is used to predict either reward port pokes irrespective of outcome (F) or rewarded pokes (G) (y-axis). Mean AUC of ROC for shuffled data (middle). Mean ± SEM AUC of ROC along the red-dashed diagonal line in (F-G), where lags indicate times to the right and left of the diagonal (right). For the predictions of rewarded pokes (G, right), AUCs were averaged specifically around the median time to reward delivery (2.8 to 3.1 seconds from the beginning of the trial). P-values generated from t-tests comparing AUCs of real data to shuffled controls for each animal (n=13 for (F), n=11 for (G), where two animals with sparse data around the median reward collection time were excluded). **(H)** AAV-hSyn:SF-iGluSnFR-184S was injected in the VTA in wild-type C57BL/6J mice and recorded after at least 3 weeks post-surgery. (**I**) Representative histology of SF-iGluSnFR expression and patch cord location. Scale bar: 500 µm. (**J**) Photometry signals for all expert trials across all animals aligned to trial start (tone on), ordered by time the animals collect reward (corresponding to the black line across all plots). Trial-wise z-scored photometry signal from SF-iGluSnFR (left, n=6 animals), iHaloGluSnFR-V2.6 (middle, n=6 animals), and iHaloGluSnFR-V2 (right, n=7 animals). iHaloGluSnFR animals are from the same dataset as in Figure 5. (**K**) Representative novice animal's single trial reward response (from their 2nd session), where t=0 is the time of reward dispense. (**L**) Mean z-scored photometry signal of SF-iGluSnFR signal aligned around rewarded or unrewarded (reward port pokes during the tone) pokes (left). AUC post reward port poke (right), where there is a reduction in glutamate for rewarded pokes compared to unrewarded for both novice ("N", **P* =0.018) and expert ("E", **P* =0.021) animals. (**M**) Z-scored photometry signal for novice and expert animals aligned to reward delivery (left), where the vertical dashed line in the left plot indicates the mean latency to poke the action port in expert trials. Signals quantified by peak increase in signal (right) pre and post reward collection. Pre-reward AUC *P* =0.28, post-reward *P* =0.85, pre-reward peak increase *P* =0.53, post-reward *P* =0.35 (iGluSnFR n=6 animals, 605 expert trials, 146 novice trials). All traces shown as mean ± SEM, and all trace quantification data shown as mean ± SD. Shapiro-Wilk tests were performed before paired t-tests. N.S. not significant *P*>0.05, **P*<0.05, ***P*<0.01, ****P*<0.001.

REFERENCES

1. Wang, J., Wang, F., Mai, D., and Qu, S. (2020). Molecular Mechanisms of Glutamate Toxicity in Parkinson's Disease. Front. Neurosci. *14*, 1–12. https://doi.org/10.3389/fnins.2020.585584.
2. Findley, C.A., Bartke, A., Hascup, K.N., and Hascup, E.R. (2019). Amyloid Beta-Related Alterations to Glutamate Signaling Dynamics During Alzheimer's Disease Progression. ASN Neuro *11*. https://doi.org/10.1177/1759091419855541.
3. Zhang, Z., Zhang, S., Fu, P., Zhang, Z., Lin, K., Ko, J.K.S., and Yung, K.K.L. (2019). Roles of glutamate receptors in Parkinson's disease. Int. J. Mol. Sci. *20*, 1–17. https://doi.org/10.3390/ijms20184391.
4. Dong, X.X., Wang, Y., and Qin, Z.H. (2009). Molecular mechanisms of excitotoxicity and their relevance to pathogenesis of neurodegenerative diseases. Acta Pharmacol. Sin. *30*, 379–387. https://doi.org/10.1038/aps.2009.24.
5. Rothstein, J.D., Martin, L.J., and Kuncl, R.W. (1992). Decreased Glutamate Transport by the Brain and Spinal Cord in Amyotrophic Lateral Sclerosis. New England Journal of Medicine *326*, 1464–1468. https://doi.org/10.1056/NEJM199205283262204.
6. Aggarwal, A., Negrean, A., Chen, Y., Iyer, R., Reep, D., Liu, A., Palutla, A., Xie, M.E., MacLennan, B.J., Hagihara, K.M., et al. (2025). Glutamate indicators with increased sensitivity and tailored deactivation rates. Nat. Methods. https://doi.org/10.1038/s41592-025-02965-z.
7. Aggarwal, A., Liu, R., Chen, Y., Ralowicz, A.J., Bergerson, S.J., Tomaska, F., Mohar, B., Hanson, T.L., Hasseman, J.P., Reep, D., et al. (2023). Glutamate indicators with improved activation kinetics and localization for imaging synaptic transmission. Nat. Methods *20*, 925–934. https://doi.org/10.1038/s41592-023-01863-6.
8. Helassa, N., Dürst, C.D., Coates, C., Kerruth, S., Arif, U., Schulze, C., Simon Wiegert, J., Geeves, M., Oertner, T.G., and Török, K. (2018). Ultrafast glutamate sensors resolve high-frequency release at Schaffer collateral synapses. Proc. Natl. Acad. Sci. U. S. A. *115*, 5594–5599. https://doi.org/10.1073/pnas.1720648115.
9. Marvin, J.S., Borghuis, B.G., Tian, L., Cichon, J., Harnett, M.T., Akerboom, J., Gordus, A., Renninger, S.L., Chen, T.W., Bargmann, C.I., et al. (2013). An optimized fluorescent probe for visualizing glutamate neurotransmission. Nat. Methods *10*, 162–170. https://doi.org/10.1038/nmeth.2333.
10. Marvin, J.S., Scholl, B., Wilson, D.E., Podgorski, K., Kazemipour, A., Müller, J.A., Schoch, S., Quiroz, F.J.U., Rebola, N., Bao, H., et al. (2018). Stability, affinity, and chromatic variants of the glutamate sensor iGluSnFR. Nat. Methods *15*, 936–939. https://doi.org/10.1038/s41592-018-0171-3.
11. Dana, H., Mohar, B., Sun, Y., Narayan, S., Gordus, A., Hasseman, J.P., Tsegaye, G., Holt, G.T., Hu, A., Walpita, D., et al. (2016). Sensitive red protein calcium indicators for imaging neural activity. Elife *5*, 1–24. https://doi.org/10.7554/eLife.12727.
12. Patriarchi, T., Mohebi, A., Sun, J., Marley, A., Liang, R., Dong, C., Puhger, K., Mizuno, G.O., Davis, C.M., Wiltgen, B., et al. (2020). An expanded palette of dopamine sensors for multiplex imaging in vivo. Nat. Methods *17*, 1147–1155. https://doi.org/10.1038/s41592-020-0936-3.
13. Fuhrmann, F., Mittag, M., Ziebarth, T., and Canziani, A. (2024). PinkyCaMP a mScarlet-based calcium sensor with exceptional brightness, photostability, and multiplexing capabilities.
14. Yokoyama, T., Manita, S., Uwamori, H., Tajiri, M., Imayoshi, I., Yagishita, S., Murayama, M., Kitamura, K., and Sakamoto, M. (2024). A multicolor suite for deciphering population coding of calcium and cAMP in vivo. Nat. Methods *21*, 897–907. https://doi.org/10.1038/s41592-024-02222-9.
15. Lee, J.D., Nguyen, A., Jin, Z.R., Moghadasi, A., Gibbs, C.E., Wait, S.J., Evitts, K.M., Asencio, A., Bremner, S.B., Zuniga, S., et al. (2024). Far-red and sensitive sensor for monitoring real time H2O2 dynamics with subcellular resolution and in multi-parametric imaging applications. Preprint, https://doi.org/10.1101/2024.02.06.579232 https://doi.org/10.1101/2024.02.06.579232.

16. Farrants, H., Shuai, Y., Lemon, W.C., Monroy Hernandez, C., Zhang, D., Yang, S., Patel, R., Qiao, G., Frei, M.S., Plutkis, S.E., et al. (2024). A modular chemigenetic calcium indicator for multiplexed in vivo functional imaging. Nat. Methods *21*, 1916–1925. https://doi.org/10.1038/s41592-024-02411-6.

17. Frei, M.S., Sanchez, S.A., Liu, L., Schneider, F., Wang, Z., Hakozaki, H., Li, Y., Lyons, A.C., Rohm, T. V., Olefsky, J.M., et al. (2024). Far-red chemigenetic biosensors for multi-dimensional and super-resolved kinase activity imaging. bioRxiv, 2024.02.10.579766.

18. Deo, C., Abdelfattah, A.S., Bhargava, H.K., Berro, A.J., Falco, N., Farrants, H., Moeyaert, B., Chupanova, M., Lavis, L.D., and Schreiter, E.R. (2021). The HaloTag as a general scaffold for far-red tunable chemigenetic indicators. Nat. Chem. Biol. *17*, 718–723. https://doi.org/10.1038/s41589-021-00775-w.

19. Grimm, J.B., Muthusamy, A.K., Liang, Y., Brown, T.A., Lemon, W.C., Patel, R., Lu, R., Macklin, J.J., Keller, P.J., Ji, N., et al. (2017). A general method to fine-tune fluorophores for live-cell and in vivo imaging. Nat. Methods *14*, 987–994. https://doi.org/10.1038/nmeth.4403.

20. Grimm, J.B., English, B.P., Chen, J., Slaughter, J.P., Zhang, Z., Revyakin, A., Patel, R., Macklin, J.J., Normanno, D., Singer, R.H., et al. (2015). A general method to improve fluorophores for live-cell and single-molecule microscopy. Nat. Methods *12*, 244–250. https://doi.org/10.1038/nmeth.3256.

21. Grimm, J.B., Tkachuk, A.N., Xie, L., Choi, H., Mohar, B., Falco, N., Schaefer, K., Patel, R., Zheng, Q., Liu, Z., et al. (2020). A general method to optimize and functionalize red-shifted rhodamine dyes. Nat. Methods *17*, 815–821. https://doi.org/10.1038/s41592-020-0909-6.

22. Tian, H., Davis, H.C., Wong-Campos, J.D., Park, P., Fan, L.Z., Gmeiner, B., Begum, S., Werley, C.A., Borja, G.B., Upadhyay, H., et al. (2023). Video-based pooled screening yields improved far-red genetically encoded voltage indicators. Nat. Methods *20*, 1082–1094. https://doi.org/10.1038/s41592-022-01743-5.

23. Mendonça, P.R.F., Tagliatti, E., Langley, H., Kotzadimitriou, D., Zamora-Chimal, C.G., Timofeeva, Y., and Volynski, K.E. (2022). Asynchronous glutamate release is enhanced in low release efficacy synapses and dispersed across the active zone. Nat. Commun. *13*. https://doi.org/10.1038/s41467-022-31070-4.

24. James, B., Darnet, L., Moya-Díaz, J., Seibel, S.-H., and Lagnado, L. (2019). An amplitude code transmits information at a visual synapse. Nat. Neurosci. *22*, 1140–1147. https://doi.org/10.1038/s41593-019-0403-6.

25. Tagliatti, E., Bello, O.D., Mendonça, P.R.F., Kotzadimitriou, D., Nicholson, E., Coleman, J., Timofeeva, Y., Rothman, J.E., Krishnakumar, S.S., and Volynski, K.E. (2019). Synaptotagmin 1 oligomers clamp and regulate different modes of neurotransmitter release. https://doi.org/10.1101/594051.

26. Mendonça, P.R.F., Langley, H., Tagliatti, E., Kotzadimitriou, D., Timofeeva, Y., and Volynski, K.E. (2024). Investigating Presynaptic Activity using the SF-iGluSnFR Sensor: Measuring Kinetics and Plasticity of Glutamate Release Across Heterogeneous Population of Synapses. In, pp. 295–319. https://doi.org/10.1007/978-1-0716-4011-1_14.

27. Barlow, S.T., Levy, A.D., Contreras, M., Anderson, M.C., and Blanpied, T.A. (2024). Dissecting the functional heterogeneity of glutamatergic synapses with high-throughput optical physiology. Preprint, https://doi.org/10.1101/2024.12.23.629904 https://doi.org/10.1101/2024.12.23.629904.

28. Dürst, C.D., Wiegert, J.S., Schulze, C., Helassa, N., Török, K., and Oertner, T.G. (2022). Vesicular release probability sets the strength of individual Schaffer collateral synapses. Nat. Commun. *13*, 6126. https://doi.org/10.1038/s41467-022-33565-6.

29. Jensen, T.P., Zheng, K., Cole, N., Marvin, J.S., Looger, L.L., and Rusakov, D.A. (2019). Multiplex imaging relates quantal glutamate release to presynaptic Ca2+ homeostasis at multiple synapses in situ. Nat. Commun. *10*, 1414. https://doi.org/10.1038/s41467-019-09216-8.

30. Jensen, T.P., Kopach, O., Reynolds, J.P., Savtchenko, L.P., and Rusakov, D.A. (2021). Release probability increases towards distal dendrites boosting high-frequency signal transfer in the rodent hippocampus. Elife *10*. https://doi.org/10.7554/eLife.62588.

31. Roshgadol, J.I., Chouinard, J.A., Majumder, S., Scott, E.C., Borges, K., Hagihara, K.M., Mancini, N., Steveson, T., Kamath, T., Lodder, B., et al. (2025). Sensitive dLight3 for imaging broad-spectrum dopamine events across brain regions. Res. Sq. https://doi.org/10.21203/rs.3.rs-7313638/v1.

32. Kotzadimitriou, D., Langley, H., McGowan, E., Mendonca, P.R.F., Tagliatti, E., Timofeeva, Y., Krishnakumar, S.S., and Volynski, K.E. (2025). Synaptotagmin-7 is required for synchronous but not asynchronous facilitation of glutamate release at cortical boutons. Preprint, https://doi.org/10.64898/2025.12.19.695358 https://doi.org/10.64898/2025.12.19.695358.

33. Aghi, K., Schultz, R., Stowers, R.S., Liu, W.Y., Mendonça, P.R.F., Li, R., Bakshinska, D., Newman, Z.L., and Isacoff, E.Y. (2025). Balanced synapse-to-synapse short-term plasticity ensures constant transmitter release. Current Biology *35*, 2881-2892.e6. https://doi.org/10.1016/j.cub.2025.05.024.

34. Newman, Z.L., Bakshinskaya, D., Schultz, R., Kenny, S.J., Moon, S., Aghi, K., Stanley, C., Marnani, N., Li, R., Bleier, J., et al. (2022). Determinants of synapse diversity revealed by super-resolution quantal transmission and active zone imaging. Nat. Commun. *13*, 229. https://doi.org/10.1038/s41467-021-27815-2.

35. Morales, M., and Margolis, E.B. (2017). Ventral tegmental area: Cellular heterogeneity, connectivity and behaviour. Nat. Rev. Neurosci. *18*, 73–85. https://doi.org/10.1038/nrn.2016.165.

36. Beier, K.T., Steinberg, E.E., Deloach, K.E., Xie, S., Miyamichi, K., Schwarz, L., Gao, X.J., Kremer, E.J., Malenka, R.C., and Luo, L. (2015). Circuit Architecture of VTA Dopamine Neurons Revealed by Systematic Input-Output Mapping. Cell *162*, 622–634. https://doi.org/10.1016/j.cell.2015.07.015.

37. McGovern, D.J., Polter, A.M., and Root, D.H. (2021). Neurochemical Signaling of Reward and Aversion to Ventral Tegmental Area Glutamate Neurons. Journal of Neuroscience *41*, 5471–5486. https://doi.org/10.1523/JNEUROSCI.1419-20.2021.

38. Amo, R., Uchida, N., and Watabe-Uchida, M. (2024). Glutamate inputs send prediction error of reward, but not negative value of aversive stimuli, to dopamine neurons. Neuron *112*, 1001-1019.e6. https://doi.org/10.1016/j.neuron.2023.12.019.

39. Van Zessen, R., Phillips, J.L., Budygin, E.A., and Stuber, G.D. (2012). Activation of VTA GABA Neurons Disrupts Reward Consumption. Neuron *73*, 1184–1194. https://doi.org/10.1016/j.neuron.2012.02.016.

40. Faget, L., Oriol, L., Lee, W.C., Zell, V., Sargent, C., Flores, A., Hollon, N.G., Ramanathan, D., and Hnasko, T.S. (2024). Ventral pallidum GABA and glutamate neurons drive approach and avoidance through distinct modulation of VTA cell types. Nat. Commun. *15*. https://doi.org/10.1038/s41467-024-48340-y.

41. Tsien, R.Y., Pozzan, T., and Rink, T.J. (1982). Calcium homeostasis in intact lymphocytes: cytoplasmic free calcium monitored with a new, intracellularly trapped fluorescent indicator. J. Cell Biol. *94*, 325–334. https://doi.org/10.1083/jcb.94.2.325.

42. Gee, K.R., Brown, K.A., Chen, W.-N.U., Bishop-Stewart, J., Gray, D., and Johnson, I. (2000). Chemical and physiological characterization of fluo-4 Ca2+-indicator dyes. Cell Calcium *27*, 97–106. https://doi.org/10.1054/ceca.1999.0095.

43. Grynkiewicz, G., Poenie, M., and Tsien, R.Y. (1985). A new generation of Ca2+ indicators with greatly improved fluorescence properties. Journal of Biological Chemistry *260*, 3440–3450. https://doi.org/10.1016/S0021-9258(19)83641-4.

44. Loew, L.M., Bonneville, G.W., and Surow, J. (1978). Charge shift optical probes of membrane potential. Theory. Biochemistry *17*, 4065–4071. https://doi.org/10.1021/bi00612a030.

45. Fluhler, E., Burnham, V.G., and Loew, L.M. (1985). Spectra, membrane binding, and potentiometric responses of new charge shift probes. Biochemistry *24*, 5749–5755. https://doi.org/10.1021/bi00342a010.

46. Mohar, B., Michel, G., Wang, Y.-Z., Hernandez, V., Grimm, J.B., Park, J.-Y., Patel, R., Clarke, M., Brown, T.A., Bergmann, C., et al. (2025). DELTA: a method for brain-wide measurement of synaptic protein turnover reveals localized plasticity during learning. Nat. Neurosci. *28*, 1089–1098. https://doi.org/10.1038/s41593-025-01923-4.

47. Zheng, Y., Cai, R., Wang, K., Zhang, J., Zhuo, Y., Dong, H., Zhang, Y., Wang, Y., Deng, F., Ji, E., et al. (2025). In vivo multiplex imaging of dynamic neurochemical networks with designed far-red dopamine sensors. Science (1979). *388*. https://doi.org/10.1126/science.adt7705.

48. Lee, J.D., Nguyen, A., Gibbs, C.E., Jin, Z.R., Wang, Y., Moghadasi, A., Wait, S.J., Choi, H., Evitts, K.M., Asencio, A., et al. (2025). Monitoring in real time and far-red imaging of H2O2 dynamics with subcellular resolution. Nat. Chem. Biol. https://doi.org/10.1038/s41589-025-01891-7.

49. Kille, S., Acevedo-Rocha, C.G., Parra, L.P., Zhang, Z.G., Opperman, D.J., Reetz, M.T., and Acevedo, J.P. (2013). Reducing codon redundancy and screening effort of combinatorial protein libraries created by saturation mutagenesis. ACS Synth. Biol. *2*, 83–92. https://doi.org/10.1021/sb300037w.

50. Liu, H., and Naismith, J.H. (2008). An efficient one-step site-directed deletion, insertion, single and multiple-site plasmid mutagenesis protocol. BMC Biotechnol. *8*, 91. https://doi.org/10.1186/1472-6750-8-91.

51. Venkatachalam, V., and Cohen, A.E. (2014). Imaging GFP-based reporters in neurons with multiwavelength optogenetic control. Biophys. J. *107*, 1554–1563. https://doi.org/10.1016/j.bpj.2014.08.020.

52. Gradinaru, V., Zhang, F., Ramakrishnan, C., Mattis, J., Prakash, R., Diester, I., Goshen, I., Thompson, K.R., and Deisseroth, K. (2010). Molecular and Cellular Approaches for Diversifying and Extending Optogenetics. Cell *141*, 154–165. https://doi.org/10.1016/j.cell.2010.02.037.

53. Shukla, N., Roelle, S.M., Suzart, V.G., Bruchez, A.M., and Matreyek, K.A. (2021). Mutants of human ACE2 differentially promote SARS-CoV and SARS-CoV-2 spike mediated infection. PLoS Pathog. *17*, 1–25. https://doi.org/10.1371/journal.ppat.1009715.

54. Edelstein, A.D., Tsuchida, M.A., Amodaj, N., Pinkard, H., Vale, R.D., and Stuurman, N. (2014). Advanced methods of microscope control using μManager software. J. Biol. Methods *1*. https://doi.org/10.14440/jbm.2014.36.

STAR METHODS

KEY RESOURCES TABLE

REAGENT or RESOURCE	SOURCE	IDENTIFIER
Antibodies		
Rabbit anti-GFP	Invitrogen	Cat#A11122, RRID: AB221569
Mouse anti-PSD95	Synaptic Systems	Cat#124011
Alexa Fluor 488 anti-c-Myc	BioLegend	Cat#626811
Donkey anti-rabbit IgG Alexa Fluor 488	Invitrogen	A11008, RRID: AB_143165
Goat anti-mouse IgG1 Alexa Fluor 633	Invitrogen	Cat#A21126, RRID: AB_2535768
Bacterial and virus strains		
NEB Stable Competent E.coli	NEB	C3040
AAV1-hSyn-iHaloGluSnFR	In-house or by UNC Neurotools	N/A
AAV1-CAG-Flex-GCaMP6s	Addgene	100842
AAV1-hSyn-SF-iGluSnFR-A184S	Addgene	106174
AAV1-ihSyn-tTA-sv40/TRE-DIO-dLight3.8	Jeff Wickens, OIST	N/A
AAV-hSyn-axon-GCaMP6s	In-house	N/A
Biological samples		
E18 Sprague Dawley rat hippocampal tissue (for dissociated neuron culture)	Transnetyx Tissue	SDEHP
Chemicals, peptides, and recombinant proteins		
NEBuilder HiFi DNA Assembly Cloning Kit	NEB	E4420S
PfuUltra II Hotstart	Agilent	600850
Platinum SuperFi II	Invitrogen	12349050
DMSO	Molecular Probes	D12345
Janelia Fluor Dye-HaloTag ligands (JF635, JF585, JF646)	Luke Lavis, Janelia	N/A
HBSS, calcium, magnesium, no phenol red	Sigma-Aldrich	H8264
Doxycycline hydrochloride	Fisher Scientific	BP26531
AP1903	ApexBio	B4168
L-glutamic acid monosodium salt monohydrate	Sigma-Aldrich	49621
GABA	Sigma-Aldrich	A5835
Dopamine hydrochloride	Sigma-Aldrich	H8502

DL-Norepinephrine hydrochloride	Sigma-Aldrich	A7256
Serotonin hydrochloride	Fisher Scientific	AAB2126303
Histamine dihydrochloride	Fisher Scientific	AC150620050
Acetylcholine chloride	Sigma-Aldrich	A2661
L-Aspartic acid monosodium salt monohydrate	Fisher Scientific	AAB2232122
CNQX	Tocris	0190
(S)-MCPG	Tocris	0337
(R)-CPP	Abcam	120159
Gabazine	Abcam	Ab120042
TTX	Tocris	1069
Pluronic F-127	Thermo Scientific	P3000MP
TFB-TBOA	Tocris	2532
Methylphenidate hydrochloride	Sigma-Aldrich	M2892
Critical commercial assays		
ZymoPURE II Plasmid Maxiprep Kit	Zymo Research	D4202
DNA Miniprep Kit	Qiagen (buffers), Syd Labs (columns)	27104 (buffers), MB082 (columns)
Wizard Magnesil Plasmid Purification System	Promega	A1635
Lipofectamine 2000	Invitrogen	11668019
Fugene6	Promega	E2691
Deposited data		
Source data	This paper	https://Figshare.com/s/22a5dfa9a8cf5aca0932
AAV-hSyn-iHaloGluSnFR	This paper	V2: Addgene #252666 V2.6: Addgene #252668 V2.7b: Addgene #252669
Experimental models: Cell lines		
HEK293T	ATCC	CRL-3216
HEK293T landing pad cells	Kenneth Matreyek, Case Western	N/A
iHaloGluSnFR HEK293T stable cell lines	This paper	N/A
Experimental models: Organisms/strains		
C57BL6/J	The Jackson Laboratory	JAX 000664
DRD1-Cre	The Jackson Laboratory	Strain #037156-JAX
Recombinant DNA		

pDisplay Mammalian Expression Vector	Invitrogen	V66020
attB-IRES-PuroR landing pad vector	Kenneth Matreyek, Case Western	N/A
pCMV-iHaloGluSnFR-PDGFR	This paper	N/A
pCMV-iHaloGluSnFR-GPI	This paper	N/A
pAAV-hSyn-iHaloGluSnFR	This paper	N/A
attB-iHaloGluSnFR-IRES-PuroR	This paper	N/A
pAAV-CAG-iGluSnFR3-GPI-v857	Addgene	178335
attB-iHaloGluSnFR-TS-Citrine-IRES-PuroR	This paper	N/A
Software and algorithms		
MATLAB	Mathworks	https://www.mathworks.com/help/install/ug/install-products-with-internet-connection.html
ThorImage	ThorLabs	v.4.3
RStudio (R)	posit	https://posit.co/download/rstudio-desktop/
Fiji	ImageJ	https://imagej.net/software/fiji/downloads
Other		
Colony picker	Singer Instruments	PIXL
Liquid Handler	Opentrons	OT2
ImageXpress Micro Confocal High-Content Imaging system	Molecular Devices	N/A
Stellaris 8	Leica	N/A
Tunable Ti:sapphire laser	SpectraPhysics	InSightX3+A
920 nm laser	Spark Lasers	ALCOR 920-2-XSight
Optical fiber Multiple Fluid Injections Cannulas	Doric Lenses	OmFC_ZF1.25_400/430-0.66_4.5mm_FLT_4.4mm_PLGS
Optofluidic cannula implant fluid injector	Doric Lenses	FI_OmFC_ZF_140/190_4.6mm, Doric Lenses

815

EXPERIMENTAL MODEL AND STUDY PARTICIPANT DETAILS

Animals

All procedures were carried out in accordance with NIH guidelines and the ethics protocol approved by respective institutions, namely UC Davis IACUC protocol #21811, and MPFI IACUC #23-004, and IACUC of the University of Pennsylvania. Experimental procedures were conducted in accordance with the Public Health Service Policy on Humane Care and Use of Laboratory Animals of the National Institutes of Health in the United States of America. The following mouse lines were used: C57BL6/J (The Jackson Laboratory, JAX 000664) and D1-cre (The Jackson Laboratory, Strain #037156-JAX). Animals were bred in-house and genotyped by Transnetyx Inc. For behavior experiments, 6–11-week-old male mice were used, and mice were housed under a reversed 12-h light/12-h dark cycle in an ambient temperature of 23 °C and 35–60% humidity. Behavioral experiments were performed during the dark phase of the cycle. For acute slice experiments, mice were group housed 2-4/cage, in standard laboratory conditions on a 12/12h light/dark cycle with ad libitum food and water. Both female and male mice at least 8 weeks of age were used for slice experiments.

METHOD DETAILS

Molecular biology

The prototype construct for iHaloGluSnFR was constructed using circular polymerase extension cloning by replacing cpGFP in iGluSnFR[9] with cpHaloTag originally from HaloTag-based calcium indicator HaloCaMP[18] in the pDisplay expression vector (Invitrogen) to create pCMV-iHaloGluSnFR-PDGFR. After the generation of V2, the PDGFR transmembrane domain was replaced by Cobl9 GPI[7] via NEBuilder HiFi DNA assembly. PCRs for cloning were conducted with either PfuUltra II Hotstart (Agilent 600850) or Platinum SuperFi II (Invitrogen 12349050), and transformations were performed with chemically competent TOP10 cells prepared in-house. pAAV-hSyn-iHaloGluSnFR constructs were constructed via restriction digest (BamHI, HindIII, NEB R3136, R3104), ligation with T4 DNA ligase (NEB M0202), and transformed in NEB Stable Competent *E. coli* (NEB C3040), cultured at 30°C. Maxipreps were performed with the ZymoPURE II Plasmid Maxiprep Kit (Zymo Research D4202).

Dye incubation of iHaloGluSnFR expressed on adherent cells

Before imaging iHaloGluSnFR-expressed adherent HEK293T (ATCC CRL-3216) or cultured neurons, dye incubation must be performed. All dyes were acquired as a gift from Dr. Luke Lavis and reconstituted in DMSO (Molecular Probes D12345) for a 1mM stock solution. A working dye concentration of 2.5 µM dye in either imaging buffer—HBSS with calcium and magnesium (Sigma-Aldrich H8264) + 20mM HEPES (Cytiva SH30237.01)-- or neurobasal plus media for neurons (Gibco A3582901) was warmed and applied to the cells. Cells were washed after ~15 min of dye incubation at

37°C in the incubator. Cells were rinsed at least 3 (neurons) or 6 (HEK293T) times with imaging buffer before imaging.

Screening

All libraries were generated using pCMV-iHaloGluSnFR variants with site-saturation mutagenesis at individual residues using degenerate primers with NNK, NDT (for reduced library sizes), or the "22c trick" to reduce codon redundancy [49]. Primers were designed based on a derivative of the QuikChange method[50] that harbor a staggered design, containing a primer-primer complementary (overlapping) region as well as a non-overlapping portion with higher T_m carrying the degenerate sequences. Primers were ordered from Integrated DNA Technologies and all PCRs for library generation were performed using PfuUltra II Hotstart PCR Master Mix (Agilent 60085) according to manufacturer's instructions. Template DNA was digested with DpnI (NEB R0176) before column purification (Qiagen 27104 buffer, columns from Syd Labs MB082). Purified PCR products were then transformed in chemically TOP10 cells prepared in-house and plated in LB agar plates with ampicillin or kanamycin at 37°C overnight. Library diversity was ascertained by pooling colonies and performing a pooled miniprep and sequenced by Genewiz (Azenta Life Sciences), where sequence trace intensities were obtained at mutated residues. Individual colonies were picked manually or by a colony picker (PIXL, Singer Instruments) in 96-well deep-well plates (Thermo Fisher AB-0932) and grown overnight in a shaking incubator at 300 RPM at either 37°C or 30°C in 2YT media with kanamycin or ampicillin.

Minipreps from 96 well cultures were performed using the Wizard Magnesil Plasmid Purification System (Promega A1635) with the OT2 robotic liquid handler (Opentrons) running a custom Python script. HEK293T were transfected with miniprepped DNA using Lipofectamine 2000 (Invitrogen 11668019) (~300 ng DNA, 0.225 uL Lipofectamine reagent, ~22,500 cells per well in a 96 well plate) performed either manually or by running a custom Python script with the OT2. Cells were imaged 2 days after transfection with the ImageXpress Micro Confocal High-Content Imaging system (Molecular Devices) using a 20x air objective in spinning disk confocal mode. Cells were incubated with dye with the aforementioned procedure and washed at least 6 times with imaging buffer (formulation above). Variants were imaged before glutamate addition, after a final concentration of 10 μM glutamate was added, and after final 100 μM glutamate addition for each well. Image analysis was performed with custom scripts in MATLAB (MathWorks). Top variants were retested by transfecting them in HEK293T cells plated in glass-bottom 4-chamber 35 mm dishes with Lipofectamine2000 and imaged by collecting time-lapse videos using the Leica Stellaris 8 confocal during 10 uM and 100 uM sequential glutamate addition.

Generation of cell lines stably expressing iHaloGluSnFR

Sensor versions were cloned into attB plasmid to generate attB-iHaloGluSnFR-IRES-PuroR plasmids. For molecular brightness measurements, the trafficking signal from Kir2.1[51,52] and Citrine was inserted to create attB-iHaloGluSnFR-TS-Citrine-IRES-PuroR plasmids. We generated cell lines stably expressing the sensors by using a HEK293T Landing Pad cell system (gift from Kenneth Matreyek, Case Western) that stably integrates single copies of the transfected transgene[53]. Recombination was achieved by transfecting HEK293T BxbI-expressing landing pad cells cultured in growth medium (GM) composed of DMEM (Gibco 11995073) with 1% penicillin/streptomycin (Sigma A5955) and FBS (Gibco 26140079) supplemented with 2 µg/mL doxycycline (Fisher BP26531). Transfection was done with Fugene6 transfection reagent (Promega E2691) in 24-well plates, as previously published, with minor modifications [7,53], https://www.matreyeklab.com/hek-293t-bxb1-landing-pad-recombinaion-protocol/1092/. 750 ng attB sensor plasmid and 2.25 µL Fugene6 transfection mix was incubated with 120,000 cells per well in a 24-well plate. After 72 hours following transfection, 1nM AP1903 (ApexBio B4168) was added for iCasp9 negative selection. 13 days after recombination, 1 µg/mL puromycin (Fisher A1113803) was added to the cells for positive selection.

Neuron culture

E18 Sprague Dawley rat hippocampal tissue was shipped fresh in Hibernate-E media from (Transnetyx Tissue SDEHP). The hippocampi were dissociated in 2 mg/mL papain (Transnetyx Tissue PAP) at 30°C for 10 min before mechanical trituration with a fire-polished pipette. The cell suspension was treated with DNAseI solution (StemCell Technologies 07469), passed through a 70 µm cell sieve (Greiner 542170) and washed once with HBSS. The cells are plated in Neurobasal Plus medium (Gibco A3582901) containing 5% FBS, 2% B27 Plus (Gibco A3582801), and 0.5 mM GlutaMAX (Gibco 35050061) in 35 mm glass bottom dishes (Cellvis D35C4-20-1.5-N or D35-14-1.5-N). Media was exchanged 24-48 hours later to the aforementioned plating media without FBS. Half media exchanges occurred every 3-4 days.

In situ characterization of iHaloGluSnFR

Dose-response curves in stably expressing HEK293T were generated by first plating 60,000 cells in the inner quadrant of glass-bottom 4-chamber 35 mm dishes (Cellvis D35C4-20-1.5-N) with DMEM growth medium supplemented with 2 µg/mL doxycycline (Fisher BP26531). Two days later, the cells were incubated with dye solution (as described above), and washed at least 6 times with imaging solution consisting of HBSS supplemented with 20 mM HEPES to remove excess glutamate. The cells were imaged with a Leica Stellaris 8 confocal with a 40x oil immersion objective. After at least three pre-ligand addition frames were acquired, two sequential glutamate (Sigma 49621) additions of 5x concentrated solutions, prepared in imaging solution, were added to the dish, allowing fluorescence response to plateau in between solutions (where dose-response curves were generated with the effective final concentrations of glutamate).

Imaging and cell preparation for *in situ* specificity tests were conducted the same as the glutamate dose-response experiments. Solutions of the following were prepared: L-Glutamic acid monosodium salt monohydrate (Sigma-Aldrich 49621), GABA (Sigma-Aldrich A5835), Dopamine hydrochloride (Sigma-Aldrich H8502), DL-Norepinephrine hydrochloride (Sigma-Aldrich A7256), Serotonin hydrocholoride (Fisher Scientific AAB2126303), Histamine dihydrochloride (Fisher Scientific AC150620050), Acetylcholine chloride (Sigma-Aldrich A2661), L-Aspartic acid monosodium salt monohydrate (Fisher Scientific AAB2232122), CNQX (Tocris 0190), (S)-MCPG (Tocris 0337), and (R)-CPP (Abcam 120159).

For 1-photon in situ spectrum generation, cells stably expressing iHaloGluSnFR were plated the day before imaging and washed at least six times with imaging solution to remove excess glutamate. Excitation and emission scans were taken before and after 100 µM glutamate addition. Excitation scans for JF635 were taken by scanning 565nm to 665nm with a white-light laser with 5 nm steps, with detectors collecting 670-790 nm emission (excitation scans for JF585: 520-620nm, detector 625-790nm; JF646: 575-675nm, detector 680-790nm). Emission scans for JF635 were performed by scanning 625nm to 725nm with 5nm spacing and 10nm bandwidth, exciting at 620nm (emission scans for JF585: 575-675nm, 570nm excitation; JF646: 635-735nm, 630nm excitation).

Neuron field stimulation and in situ dose-response curve

E18 rat hippocampal neurons were transduced with AAV1-hSyn-iHaloGluSnFR made in-house or by UNC Neurotools on DIV5-7 and imaged DIV11-14 for neuronal field stimulation. Stimulation was carried out by fitting dishes with a RC-37FS perfusion insert (Warner Instruments) and imaged in neuron imaging buffer (145 mM NaCl, 2.5 mM KCl, 10 mM Glucose, 10 mM HEPES, 2 mM $CaCl_2$ and 1 mM $MgCl_2$, pH 7.3) at room temperature with a synaptic inhibitor cocktail consisting of 10 µM CNQX, 10 µM (R)-CPP, 10 µM Gabazine (Abcam AB120042), and 500 µM (S)-MCPG. 4V field stimulation trains were applied at 30 Hz. Images were acquired using resonant scanning (12 ms/frame) with the Leica Stellaris 8 with the 40x oil immersion objective. 3 replicates of each stimulation were performed for each ROI.

For *in situ* neuron titrations, neurons plated in 4-chamber 35mm dishes were transduced with AAV1-hSyn-iHaloGluSnFR DIV8-12 and imaged DIV16-18. After 15 min dye incubation at 37°C as detailed above, cells were rinsed 4 times and imaged in neuron imaging buffer with a synaptic inhibitor cocktail to silence network activity (formulation above). A single glutamate addition of 5x concentrated glutamate was added per quadrant following recording at least 3 frames of a pre-ligand addition baseline, with dose-response curve concentrations reported as the effective final concentration of glutamate after ligand addition in each well.

Image analysis for in situ characterization

Analysis of images acquired for sensor screening and characterization were analyzed by custom MATLAB scripts and visualized and statistically analyzed via custom R scripts. For screening data, images were first registered via SIFT alignment using Fiji. Images for screening data taken via widefield microscopy were background subtracted by subtracting all pixel values with the average intensity of the dimmest 3x3 pixel region in the image. Masks for quantification were determined by employing Canny edge detection to outline cell membranes on either the maximum intensity projection (for confocal images) or the image taken after ligand application (for widefield images/screening data), after which saturated pixels were excluded from the mask. For *in situ* characterization data, this mask was further refined by only including the 25% brightest pixels in the mask which we determined to closely outline sensor-expressing membrane. ΔF/F was calculated by the average of pixels within this mask on individual frames of the image, dividing by the average of the pixels in the mask applied on the average of all baseline images (at least 3 frames for confocal experiments, or the pre-ligand frame for widefield experiments), subtracted by 1. For one-photon characterization data, fluorescence values across wavelengths were divided by maximum mean intensity within the mask for each culture.

For ligand addition experiments, reported ΔF/F at each concentration were taken by averaging the ΔF/F of at least three frames upon reaching steady-state. All dose-response curves were fitted to a four-parameter log-logistic Hill equation with a slope of 1 and a fixed minimum response of 0 using drc::LL.4(-1, 0, NA, NA) in R. S-slope was determined by dividing the derived E_{max} (expressed as a percentage) by the EC50. Parameter estimates with their standard errors are reported. Molecular brightness images were analyzed as above and values were determined by dividing mean iHaloGluSnFR fluorescence by mean Citrine fluorescence within the mask, where the mask was determined from the mean of three frames (of the iHaloGluSnFR channel) post glutamate addition. For neuron field stimulation experiments, analysis was done as above, but masks for quantification were derived by performing Canny edge detection on the average projection of the image stack with saturated pixels excluded and further refined by keeping the brightest 70% of pixels within the mask. For neuron field stimulation decay kinetics characterization, fluorescence decay $t_{1/2}$ was derived by fitting the initial decay ΔF/F trace from 1AP stimulation (either 2.5 or 5 seconds from stimulation onset) averaged across stimuli replicates (3 per stimuli type/sample), with a double exponential decay function with custom MATLAB scripts, where the fast decay component is reported. Rise $t_{1/2}$ were estimated by the first timepoint from stimulation at which the fluorescence signal reaches at least half of its peak (likely overestimating the $t_{1/2}$ because of the limited acquisition speed). Peak signal-to-noise ratio (SNR) was determined by dividing the peak ΔF/F of raw ΔF/F traces for each sample by the standard deviation of the baseline trace (-1.5 to -0.5 seconds before stimulation onset of the raw ΔF/F trace). Reported SNRs are average SNRs across the three stimulation replicates for a given cell/ROI.

Optical mini assay

Optical mini assays were carried out as previously published[7] with modifications. Cultured neurons were transduced DIV10 with AAV1-hSyn-iHaloGluSnFR or AAV-CAG-iGluSnFR3-GPI-v857 (plasmid acquired from Addgene 178335), with virus produced in-house, and imaged DIV19-20. After dye incubation (for iHaloGluSnFR), cells were rinsed three times with the above neuron imaging buffer, with 4mM $CaCl_2$. Cells were incubated with 2 μM TTX (Tocris 1069) before addition of 100 mM sucrose, after which optical minis were imaged. Images were acquired with the Leica Stellaris 8 using resonant scanning (12 ms/frame, 83.3 Hz) and a 40x oil immersion objective. Analysis was performed using optical mini analysis MATLAB code published in Aggarwal, et al[7]. For trace analysis, peaks were identified with findpeaks(), and the fluorescence decay of individual release events was fit to a double exponential decay function, where the fast component of the fit was reported.

Quantal analysis

Primary mouse hippocampal cultures were sparsely transfected with pAAV-hSyn-iHaloGluSnFR-V2.6 plasmid at DIV 5 using Lipofectamine 2000 (Invitrogen). At DIV14-21, neuronal culture coverslips were incubated with 2.5uM JF585 dye for approximately 20 minutes, then gently washed and transferred to the recording chamber mounted on an IX73 inverted microscope (Olympus).

Neuronal cultures were maintained in extracellular solution composed of (in mM): 139 NaCl, 2.5 KCl, 10 HEPES, 10 D-glucose, 2 CaCl2, 1.3 MgCl2 (pH 7.3 balanced with NaOH). Synaptic blockers AP5 50μM, NBQX 10μM and Gabazine 20μM were added to the bath to silence network activity. Recordings were performed at room temperature. Electrophysiological data was acquired with an Axopatch 200B amplifier and Digidata 1440A (Molecular Devices) controlled by WinWCP software (Developed by John Dempster, University of Strathclyde). Borosilicate glass pipettes (Warner Instruments) with resistance 4-7 MΩ were used for whole-cell voltage-clamp recordings. Intracellular solution was composed of (in mM): 105 K+ Gluconate, 30 KCl, 10 HEPES, 10 Phosphocreatine- Na_2, 4 ATP-Mg, 0.3 GTP-NaH_20, 0.1 EGTA (pH=7.3, balanced with KOH, 284 mOsm).

A region of interest (ROI) with dense axonal arbor was selected for high-speed imaging using a 40x oil objective. iHaloGluSnFR-JF585 was imaged using the 550 nm line from a pe400^{max} LED system (CoolLED), with a 559/34nm band pass excitation filter and a 630/69 band pass emission filter. Images were acquired at 125 fps (8 ms exposure) using a Kinetix sCMOS camera (Photometrics) and μmanager software[54]. The LED output was triggered by the camera exposure to reduce photobleaching. Action potentials were evoked in voltage-clamp mode, using 5ms depolarizing pulses from -70mV to 10mV, which produced characteristic inward escape currents. Stimulation was evoked at 5 Hz x 50 action potentials or with a total of 10 paired action potentials at 20Hz.

Quantal analysis was performed as previously described [23,26]. Briefly, the image stack was first Gaussian bandpass-filtered between 0.2 Hz and 20 Hz to enhance iHaloGluSnFR transients. Next, a maximal projection was extracted from the filtered image stack, revealing all presynaptic boutons that displayed activity during 5 Hz stimulation. Raw fluorescence traces were deconvolved with a single quantum waveform (τ_{decay} = 82ms). Events for analysis were determined by selecting peaks from deconvolved traces that exceeded 4 standard deviations from the baseline. Histograms of event amplitudes were fitted with a multi gaussian function to distinguish single and multi-quantal events. 20 Hz paired pulse stimulation was also performed for individual boutons, where $PPR_{optical} = 2Q_2/(Q_1 + Q_2)$, and Q_1 and Q_2 are the sums of the quantal content for the first and second action potentials.

Viral injections

AAV1 particles for pAAV-hSyn-iHaloGluSnFR-V2-GPI and pAAV-hSyn-iHaloGluSnFR-V2.6-GPI were packaged, purified, and concentrated by the University of North Carolina Neurotools. AAV1-CAG-Flex-GCaMP6s (Addgene 100842-AAV1), AAV-Syn-axon-GCaMP6s (produced in-house), and AAV1-ihSyn-tTA-sv40/TRE-DIO-dLight3.8 (gift from Jeff Wickens, OIST) were also used.

For surgery, mice were anesthetized in an induction chamber (3–4% isoflurane) and placed into a stereotaxic frame (Kopf Instruments, 1900) where they were maintained at 1–2% isoflurane. Stereotaxic injections were performed on C57Bl6/J and D1-Cre homozygous mice under aseptic conditions using isoflurane anesthesia and an inserted glass micropipette pulled to a long narrow tip (Narishige PE-22, Japan) mounted on a nanoinjector (Drummond Nanoject III). Animals were anesthetized with isoflurane gas (induction, 3.0%; supplemental, 2.0%). The heads were positioned in a stereotaxic frame (David Kopf Instruments, model 942) with non-ruptured ear bars. Ophthalmic ointment was applied to the cornea to prevent desiccation. The scalp was first shaved (first with clipper, then shaving cream) and cleaned. The skin was disinfected with 0.2% chlorhexidine gluconate antiseptic solution alternated with alcohol wipes before beginning the surgery. To expose the skull, a small incision (~1.5 cm) was made with a sterile surgical scalpel along the medial line through the skin. The connective tissue on top of the skull were removed to assure clear viewing of the stereotaxic markers and the position of the head was adjusted so that the height of the skull surface at bregma and lambda was the same. A craniotomy of 1-2 mm diameter was performed under the guidance of stereotaxic coordinates using a motorized drill. 400-800 nL of AAV virus preparation were injected at an infusion rate of 2nL/s. Injections coordinates are as follows: for CA3-CA1, CA1 (AP -1.8, ML 1.5, DV -1.65 from bregma), CA3 (AP -1.75, ML -2.34, DV -2.45 from bregma), dorso-lateral striatum (AP 1.0 mm and ML -2.0 mm from bregma, with DV -2.2 from pia). For photometry, AAV viruses (0.5–1 µL total volume) were unilaterally injected into the VTA (from bregma, anteroposterior (AP), −3.06 mm; mediolateral (ML), ±0.6 mm and dorsoventral (DV), −4.2 mm from the surface of cortex) through a pulled glass pipette at a rate of 0.2 µL min^{-1}. For the systemic dye delivery study, 400 nL virus was injected into the PAG (AP -4.6, ML +0.7, DV -2.6) and ACC (AP +1.5, ML +0.3, DV -1.6). During injection, the animals' body temperature was maintained at 37°C throughout the procedure using a heating pad system with a feedback loop temperature controller (55-7030, Harvard Apparatus). Animals were given 5mg/kg sc injection, buprenorphine ER 1mg/kg sc, before the end of surgery, and painkiller was provided in food (Rimadyl MD150-2, Bio-Serv USA) for 72-hours post-injection. Animals were used after at least 3 weeks post-injection.

Slice preparation, dye incubation, and imaging

Animals were deeply anesthetized with isoflurane and decapitated. Brains were quickly extracted and chilled for about 30-60 sec in ice-cold cutting artificial cerebrospinal fluid (ACSF) solution composed of 92 mM NMDG, 2.5 mM KCl, 1.25 mM NaH_2PO_4, 30 mM $NaHCO_3$, 20 mM HEPES, 25 mM D-Glucose, 2 mM thiourea, 5 mM Na-Ascorbate, 3 mM Na-Pyruvate, pH adjusted to 7.38-7.4, supplemented with 0.5 mM CaCl2 and 10 mM MgCl2, and gassed with carbogen (95% O_2, 5% CO_2). Brains were then quickly placed on filter paper bathed in cutting ACSF. DLS brain hemispheres were separated with a razor blade, turned to place the midline sides down and cut in an oblique plane 45° rostral-up to the horizontal to preserve corticostriatal fibers. Oblique 45-degree slices (300 µm thick) were cut using a vibratome (VT1200S, Leica) along the striosomes in ice cold oxygenated cutting ACSF. For acute slices for imaging other brain regions, coronal sections were prepared. After cutting, slices were immediately transferred into a holding chamber filled with carbogenated cutting ACSF at 34°C, ≤12 min, for recovery. Slices were then transferred in 100 µm cell strainers (431752, Corning) in a 6-well plate where they were incubated for 1 hour at room temperature with carbogen perfused 5 uM dye solution prepared by solubilizing 100 nmol JF635 or JF585 HaloTag ligand with 20 µL DMSO, 20 µL Pluronic F-127 (Thermo Scientific P3000MP), and 20 mL holding ACSF. Slices were then rinsed 3-4 times with holding ACSF for a total of 1 hour following dye incubation to wash out unbound dye. Afterwards, slices were kept in a new chamber (BSK-4, Autom8, Scientific) filled with carbogen perfused holding ACSF (92 mM NaCl, 2.5 mM KCl, 1.25 mM NaH2PO4, 30 mM NaHCO3, 20 mM HEPES, 25 mM d-Glucose, 2 mM Thiourea, 5 mM Na-Ascorbate, 3 mM Na-Pyruvate, pH adjusted to 7.35-7.4 and supplemented with 2 mM $CaCl_2$ and 2 mM $MgCl_2$, 300 mOs) at room temperature until imaged.

2-photon imaging of acute slice

Imaging was carried out in carbogenated recording ACSF (119 mM NaCl, 2.5 mM KCl, 1.25 mM NaH2PO4, 24mM NaHCO3, 12.5 mM D-Glucose, pH adjusted to 7.35-7.4 and supplemented with 2 mM CaCl2 and 2 mM MgCl2 for a solution adjusted around 295-300 mOs) at about 29°C using a 2-

photon microscope. iHaloGluSnFR was excited at 1100nm when bound to JF585 HaloTag ligand and 1200nm for JF635 HaloTag ligand with an AOM Tunable Ultrafast Ti:sapphire laser (SpectraPhysics, InSightX3+A), while dLight or GCaMP were excited at 920nm with a fixed wavelength compact femtosecond laser (Spark Lasers, ALCOR 920-2-XSight). For 2-photon spectra, stable cells expressing the sensor bound to dye were excited in imaging buffer from 740nm to 1300nm with 10nm spacing. Images were obtained with an Olympus 25X, 1.05NA water immersion objective and emitted fluorescence was detected with 3 GaAsP photomultipliers (Hamamatsu, PMT2100R) separated by a dichroic 562LP, 525/50nm filter for GFP, dichroic 635 and 607/70nm filter for JF585, and 647LP filter for JF635. Data was acquired and collected using ThorImage 4.3. Images after TBOA (Tocris 2532) and/or methylphenidate (Sigma-Aldrich M2892) application were taken after 15 minutes following drug infusion.

Electrically-evoked phasic neuromodulator release was achieved with 40 Hz trains of stimuli (pulse width 0.2 ms; 10 V) delivered through a bipolar stimulating electrode (Array of 2 SNEX-100 PI concentric electrodes epoxied side-by-side, Microprobes, MD, USA) connected to an analog stimulus isolator on bipolar mode, range 1V/V (Model 2200, A-M Systems) controlled by Axon Digidata 1550B and triggered by a custom program ran with pCLAMP (Molecular Devices, Version 10.7.03). Experiments were carried out at a scan rate of 33 Hz (512 × 512 pixels).

2-photon image analysis

All 2p image analysis was performed using custom MATLAB scripts. Briefly, masks for $\Delta F/F$ calculation were determined by taking the average projection image binarized with adaptive imbinarize() and further refined to remove dim pixels and outlier bright pixels (corresponding to noise or debris). V2 data was acquired with different imaging conditions, and masks were determined by using the maximum dF image (maximum image subtracted by average of baseline) of the image stack after downsampling 8x, and performing edge detection. $\Delta F/F$ traces were calculated using mean intensities within the mask at a given timepoint, and on the average projection image of the pre-stimulation frames. Peak response values were derived from $\Delta F/F$ traces, and decay $t_{1/2}$ were determined by fitting the $\Delta F/F$ traces between its peak and 4 seconds after the peak with a biexponential decay function plus a baseline offset. For noisy traces, the raw trace was smoothed with a 5 point moving average filter. All reported $t_{1/2}$ utilize the fast decay component of the fit and are derived from fits only when $R^2>0.7$.

For correlation analysis between bouton Axon-GCaMP and iHaloGluSnFR-V2.6 signal, first images were averaged across the 3 replicates of 5 pulse stimulation per ROI. The image stacks were then temporally downsampled 5x and the frame with the maximum intensity was used to calculate pixel-wise $\Delta F/F$, where the baseline was defined as the first 8 frames of the downsampled, averaged image stack. The pixel-wise $\Delta F/F$ image was used for mask creation, where after median filtering, the image was binarized with adaptive thresholding and segmented with watershed() using MATLAB's Image Segmenter. Then, bwconncomp() was used to detect connected components, and bouton masks were filtered for appropriate area and circularity. A label matrix was constructed out of the segmented image and used as masks to quantify the peak ΔF/F within each labelled mask. Then the averaged (across stimulation replicates) image stack was used as inputs to calculate peak ΔF/Fs either within the bouton ROI (for GCaMP images) or using ring ROIs of 5 pixel width around each bouton, from 0 to 8.91 μM (up to 75 dilations) from the bouton with a 0.594 μM (5 pixel) step size for iHaloGluSnFR image stacks. Then the Pearson's correlation was calculated between peak ΔF/Fs of GCaMP and corresponding iHaloGluSnFR ring responses. Heatmaps and correlation analysis were generated with custom R scripts.

2p spectrum image analysis was performed as previously described for *in situ* characterization, where masks are determined by the maximum intensity projection of pictures taken across all wavelengths and the mean fluorescence was determined within the mask. Average intensities were normalized by laser power at the given wavelength squared, and divided by the maximum normalized fluorescence of all the wavelengths for the sample.

Systemic dye delivery

Four weeks after viral injections, mice received intrathecal (two 10uL injections, one hour apart) or retroorbital (two 30uL injections, one hour apart) administration of JF646. 100nmol of each dye was reconstituted with 20uL DMSO (Sigma-Aldrich, D2653-5X5ML), 20uL Pluronic-F127 (Thermo Scientific P3000MP), and 60uL 1X PBS. Four hours after the first dye injection, mice were intracardially perfused with 1X PBS, followed by 4% PFA (Avantor, 100504-858). Brains were post-fixed in 4% PFA for 24 hours and then transferred to 30% sucrose until sunk. Brains were cryosectioned at 30uM. For visualization of cells labeled with JF dyes, slices were imaged with only DAPI staining. For visualization of dye overlap with viral expression, tissue underwent immunohistochemistry with Alexa Fluor 488-conjugated anti-c-Myc antibody (BioLegend, 626812, used at 1/100) according to instructions in the Promega technical manual 'HaloTag® Technology: Focus on Fluorescent Imaging with DMSO-Soluble Ligands'.

Optofluidic implant surgery and dye infusion for fiber photometry

Optical fiber implantation was performed using Optical fiber Multiple Fluid Injections Cannulas (Doric Lenses, OmFC_ZF1.25_400/430-0.66_4.5mm_FLT_4.4mm_PLGS). The fiber tips were placed 100 to 200 μm above the injection site, and the implant was secured to the skull using dental cement (Parkell). Behavioral experiments were conducted 4–7 weeks after viral injection. Dye was prepared as previously reported-- 100 nmol dye was reconstituted in 20 μL of DMSO, to which 20 μL Pluronic F-127 (Thermo Scientific P3000MP) and 60 μL PBS was added[19]. Dye was infused with a syringe pump

(RWD R462) with a 2 µL Hamilton syringe (Millipore Sigma) connected to the implant fluid injector (Doric Lenses, FI_OmFC_ZF_140/190_4.6mm). 1 µL dye was infused at 0.1 µL/min for 10 min, followed by a 5 min rest period after which the injector was removed. Dye infusion was performed 5-6 hours before recording.

Operant reward learning task

Mice were initially water deprived up to 90% of their body weight and patch cord habituated for 2 days in their home cage before being trained in an operant learning paradigm for a total of 1-14 days with a custom-built modular test chamber (17.8 × 15.2 × 18.4 cm) controlled by Arduino Uno microcontrollers before recording. Mice were tethered to a photometry cable and habituated to an operant chamber in which there is an action port and reward port. At the beginning of each trial, an auditory cue (speaker) was presented. The trial began when the mouse engaged with the action port for a minimum of 150 ms, after which the speaker turned off. Following action port engagement and the tone turning off, the mouse could poke the reward port, receiving a water reward upon successful interaction (approximately 2.6 µL per drop). Trials were separated by a randomized inter-trial interval (ITI), with a duration ranging between 10 and 20 seconds, before the next session commenced. Novice animals were recorded in the first or second session in the operant chamber, and expert animals were trained for at least 7-11 days before recording.

Fiber photometry recording and analysis

Fiber photometry was conducted using a CMOS-based Doric bundle-imaging fiber photometry system. For dual color imaging, alternating 490nm and 630nm excitation light was delivered at 20 Hz through 400 µm core 0.57 NA low autofluorescence patch cords (BBP(5)_400/430/1100-0.57_2.5m_SMA-5xZF1.25_LAF, Doric Lenses Inc.). For iGluSnFR animals, 490nm light was delivered at ~60 Hz. Emission light was collected with 2 CMOS cameras (GFP: 503-540+577-614 nm, iHalo-V2.6-JF635 660-735nm).

Photometry traces were analyzed by custom Python scripts. The raw fluorescence trace was subtracted by a 5th order polynomial fit to correct for slow baseline drifts and photobleaching. The data was chunked into trials corresponding to 5 seconds before the speaker turns on to the 5 seconds before the start of the next instance of the speaker turning on. Z-scores were determined on trial-chunked data by subtracting the baseline corrected fluorescence signal with the mean of the signal during the 2 second window preceding the start of a trial, divided by the standard deviation of the signal during the baseline time window. Peri-event Z-scores were determined similarly, where the baseline window is -2.5 to -1.5 seconds before the behavioral event within each trial. Alignments to unrewarded pokes were only included if spaced at least 2 seconds apart from the previous poke to the reward port where no water is delivered. For peri-event analyses, we used the fastest 80% of expert trials across animals to ensure the expert data captures learned, voluntary behavior. Analysis and visualization of the data were performed with custom R scripts. AUCs were determined with pracma::trapz() on peri-event z-scored traces. Peak magnitudes were determined by first determining local minima and maxima of the signal at -2 to 0 seconds (for pre-event calculations) or 0 to 2 seconds (for post-event calculations) for z-scored traces averaged by animal using pracma::findpeaks(). Peak magnitudes were determined by calculating the maximum increase in signal between neighboring local extrema (including signal edges) of signals smoothed with sgolayfilt(p=3, n=19). Cross-correlation analysis between dLight and iHaloGluSnFR signals were performed on demeaned, smoothed (rolling average window of 250 ms with slider::slide_dbl()), trial-wise Z-scored traces aligned to speaker on (the entire trial) or the -2 to +2 seconds around reward delivery using ccf() with time lags of -2.5 to 2.5 seconds where the Halo signal is shifted with respect to the dLight signal. Note that since photometry acquisition of dLight and iHaloGluSnFR were interleaved (taken 25 ms apart from each other), but were aligned assuming signals were acquired simultaneously, there is a 25 ms technical uncertainty in the lag estimates.

Logistic regression analysis was carried out using scikit-learn, where single trial photometry and behavior data (either rewarded pokes, or reward port pokes irrespective of outcome) for each animal were binned into 200 ms time bins. 4 bins of photometry signal (800ms) were used to predict either reward port poke or reward dispense and slid across time with 1 bin steps. Models were trained with L2 regularization and stratified shuffle-split cross-validation was implemented (100 splits, 50% test set). ROC AUC was averaged across animals and further quantified by determining mean AUC across lag times from the diagonal (with matched behavior and photometry time points) either across all timepoints, or specifically around the median time to reward delivery (2.8 to 3.1 seconds) due to the sparsity of rewarded pokes across trials. Shuffled controls for each animal were generated by randomly shuffling photometry trial identity.

Histology for acute slice and fiber photometry

Mice that had been recorded were anesthetized in an induction chamber (3–4% isoflurane) followed by transcardial perfusion with ice-cold 1× PBS and subsequently perfused with ice-cold 4% paraformaldehyde in 1× PBS. After extraction of the mouse brains, samples were post-fixed in 4% paraformaldehyde at 4°C overnight. The mouse brains were cryo-protected by immersion in 30% sucrose in a 1× PBS solution for three successive days. Samples were then transferred to a −80 °C freezer for long-term storage or were sliced into 50-μm sections on a microtome (Leica Biosystems) for fiber photometry histology, and 30- μm sections for post-hoc acute slices. Slices were blocked with 10% NGS 0.3% Tween-20 for 1 hour before staining with rabbit anti-GFP primary antibody (Invitrogen A11122) with or without mouse anti-PSD95 antibody (Synaptic Systems Cat#124 011) overnight at 4°C, washed and incubated with donkey anti-Rabbit Alexa Fluor 488 secondary antibody (Invitrogen A11008) with or without anti-Mouse IgG1 Alexa Fluor 633 (Invitrogen A21126). Slices were mounted with Prolong Diamond mounting medium (Molecular Probes P36966) and imaged on Leica DMi8, Nikon Eclipse Ji, or Leica Stellaris 8. Imaris (Oxford Instruments) was used for generating 3D reconstructions of histology images.

QUANTIFICATION AND STATISTICAL ANALYSIS

Image and photometry signal quantification was performed as described above, with code deposited on FigShare (https://Figshare.com/s/22a5dfa9a8cf5aca0932). All statistical tests were performed using R. For sensor characterization data, Kruskal-Wallis Rank Sum tests using kruskal.test(x, y) was conducted followed by a Dunn's *post-hoc* test for pairwise comparisons with the Holm correction using rstatix::dunn_test(x, y, p.adjust.method="holm")), where P<0.05 was considered significant.. For examining drug effects in acute slice or for fiber photometry data, Shapiro-Wilk tests were performed with shapiro.test, where normality was assumed for p>0.01, followed by paired t-tests using t.test(paired=TRUE), rstatix::pairwise_t_test, or visualized with ggpubr::stat_compare_means(method="t.test", paired=TRUE), where P<0.05 was considered significant. Significance is denoted by N.S. *P* >0.05, * *P* <0.05, ** *P* <0.01, and *** *P* <0.001. Data are represented as either mean ± SEM or mean ± SD, as specified in the figure or table legends.

SUPPLEMENTAL INFORMATION

Table S1. Titration data in HEK293T stable cell lines or AAV-transduced neurons. Shown as mean ± SEM.

Table S2. AAV-transduced neuron whole field stimulation characterization. Shown as mean ± SEM.

Table S3. 2-photon acute slice stimulation characterization of iHaloGluSnFR. Shown as mean ± SD.

Table S4. Bouton release profile of all boutons labeled in Figure 3B, including total quanta released, release rate (Pr), and optical paired-pulse ratio (PPR).

Data S1: Sequence alignment for main versions of iHaloGluSnFR.

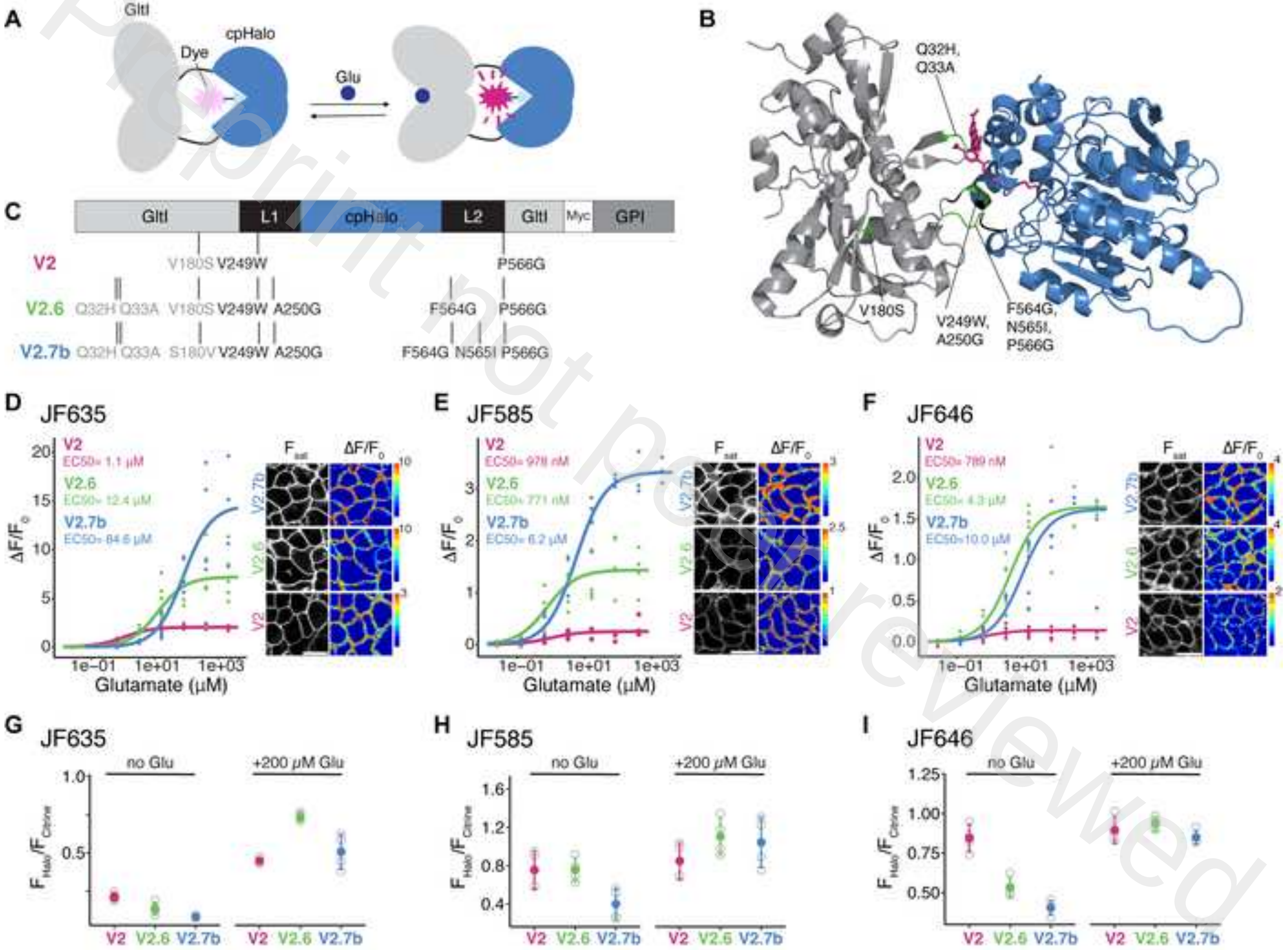
A
GltI
Dye
cpHalo
Glu
B
Q32H,
Q33A
V180S
V249W,
A250G
F564G,
N565I,
P566G
C
GltI
L1
cpHalo
L2
GltI
Myc
GPI
V2
V180S V249W
P566G
V2.6
Q32H Q33A V180S V249W A250G
F564G P566G
V2.7b
Q32H Q33A S180V V249W A250G
F564G N565I P566G
D
JF635
V2
EC50= 1.1 µM
V2.6
EC50= 12.4 µM
V2.7b
EC50= 84.6 µM
ΔF/F0
Glutamate (µM)
1e−01
1e+01
1e+03
Fsat
ΔF/F0
V2.7b
V2.6
V2
E
JF585
V2
EC50= 978 nM
V2.6
EC50= 771 nM
V2.7b
EC50= 6.2 µM
ΔF/F0
Glutamate (µM)
F
JF646
V2
EC50= 789 nM
V2.6
EC50= 4.3 µM
V2.7b
EC50=10.0 µM
ΔF/F0
Glutamate (µM)
G
JF635
no Glu
+200 µM Glu
FHalo/FCitrine
V2 V2.6 V2.7b
V2 V2.6 V2.7b
H
JF585
no Glu
+200 µM Glu
FHalo/FCitrine
I
JF646
no Glu
+200 µM Glu
FHalo/FCitrine

Figure 2

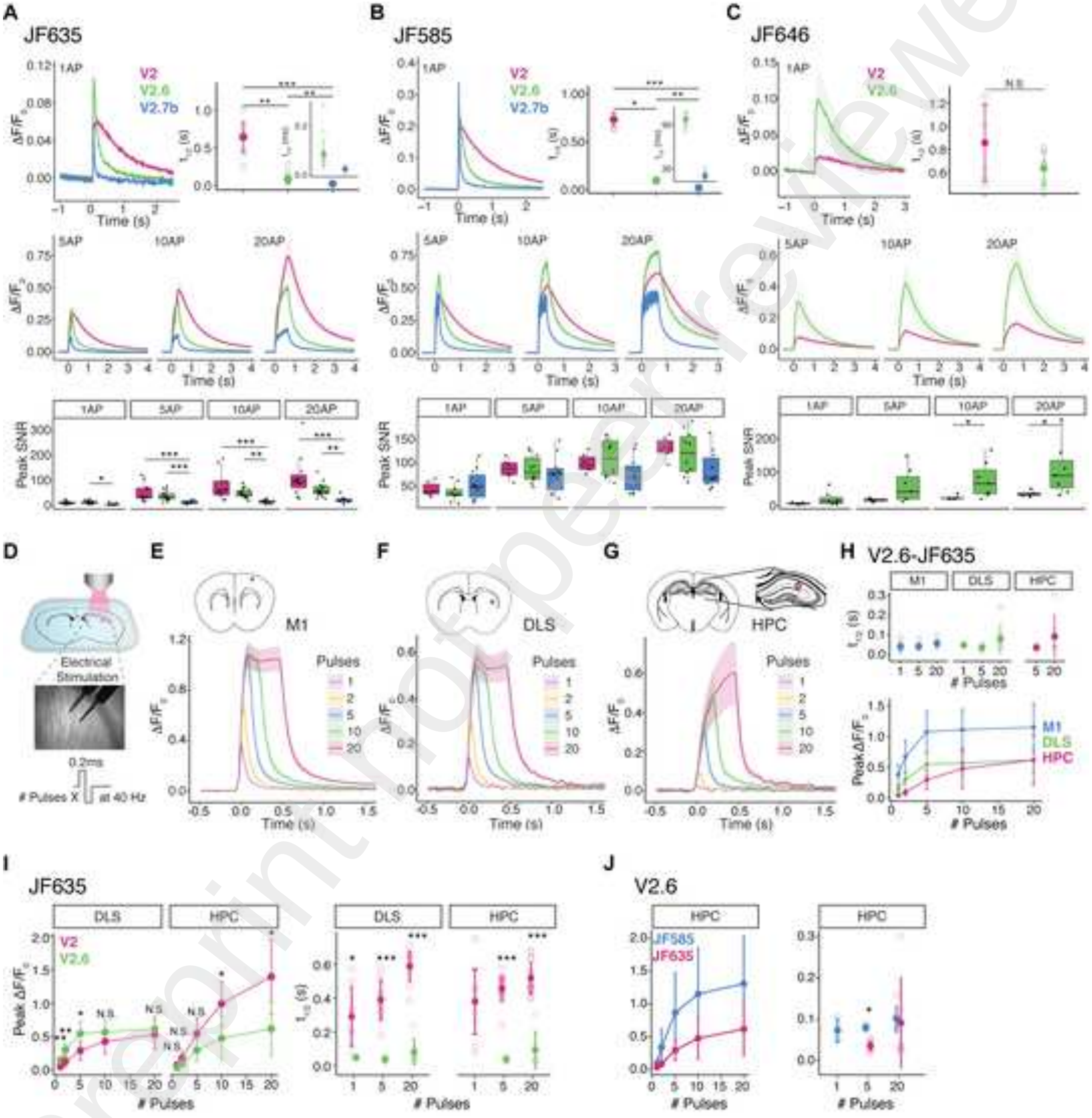
A
JF635
1AP
V2
V2.6
V2.7b
ΔF/F₀
Time (s)
$t_{1/2}$ (s)
5AP
10AP
20AP
Peak SNR
B
JF585
C
JF646
N.S
D
Electrical Stimulation
0.2ms
Pulses X at 40 Hz
E
M1
Pulses
1
2
5
10
20
F
DLS
G
HPC
H
V2.6-JF635
M1
DLS
HPC
Pulses
Peak ΔF/F₀
I
JF635
V2
V2.6
J
V2.6
HPC
JF585
JF635

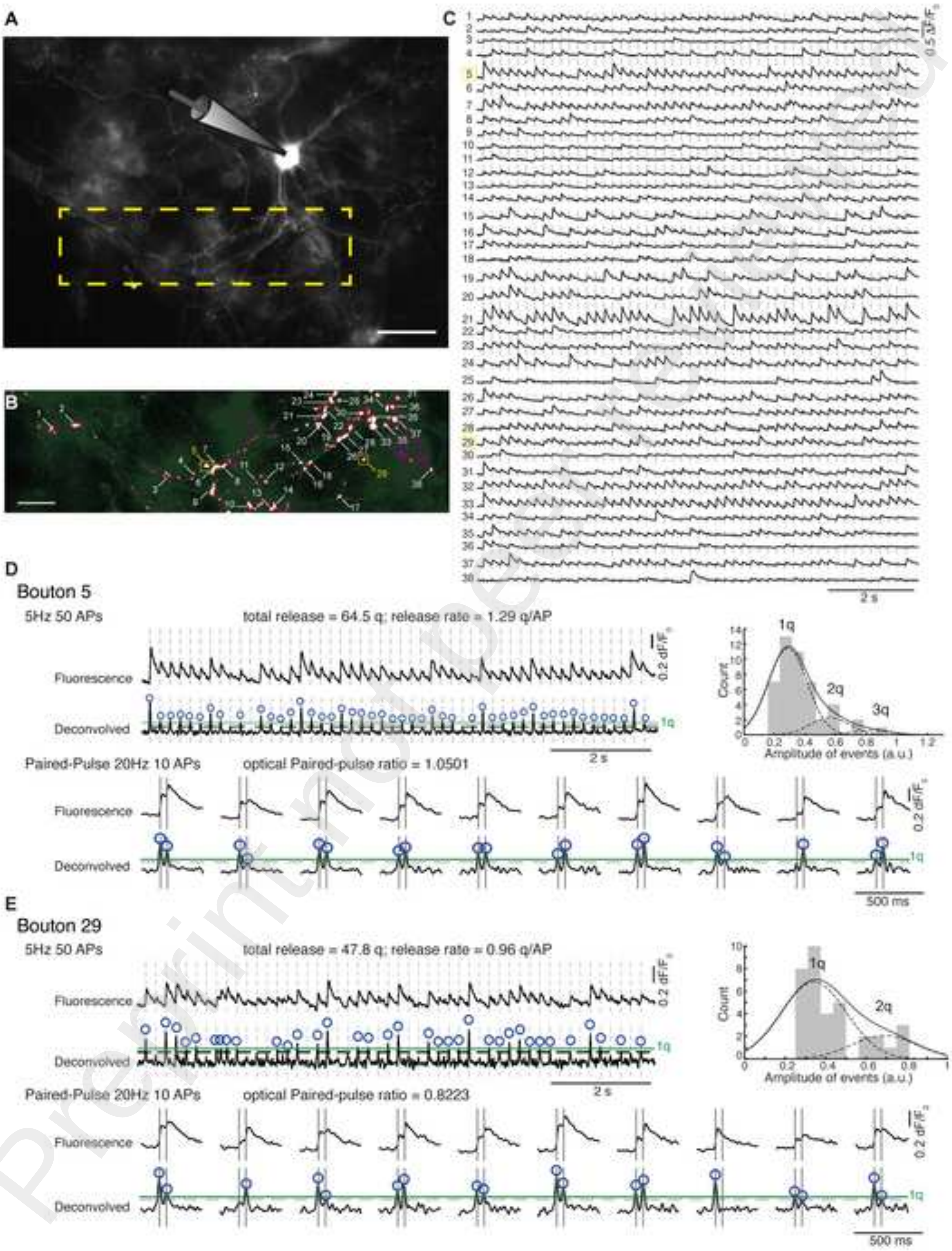
A
B
C
0.5 ΔF/F0
2 s
D
Bouton 5
5Hz 50 APs
total release = 64.5 q; release rate = 1.29 q/AP
Fluorescence
Deconvolved
0.2 dF/F0
1q
2 s
1q
2q
3q
Count
Amplitude of events (a.u.)
Paired-Pulse 20Hz 10 APs
optical Paired-pulse ratio = 1.0501
Fluorescence
Deconvolved
0.2 dF/F0
1q
500 ms
E
Bouton 29
5Hz 50 APs
total release = 47.8 q; release rate = 0.96 q/AP
Fluorescence
Deconvolved
0.2 dF/F0
1q
2 s
1q
2q
Count
Amplitude of events (a.u.)
Paired-Pulse 20Hz 10 APs
optical Paired-pulse ratio = 0.8223
Fluorescence
Deconvolved
0.2 dF/F0
1q
500 ms

Figure 4

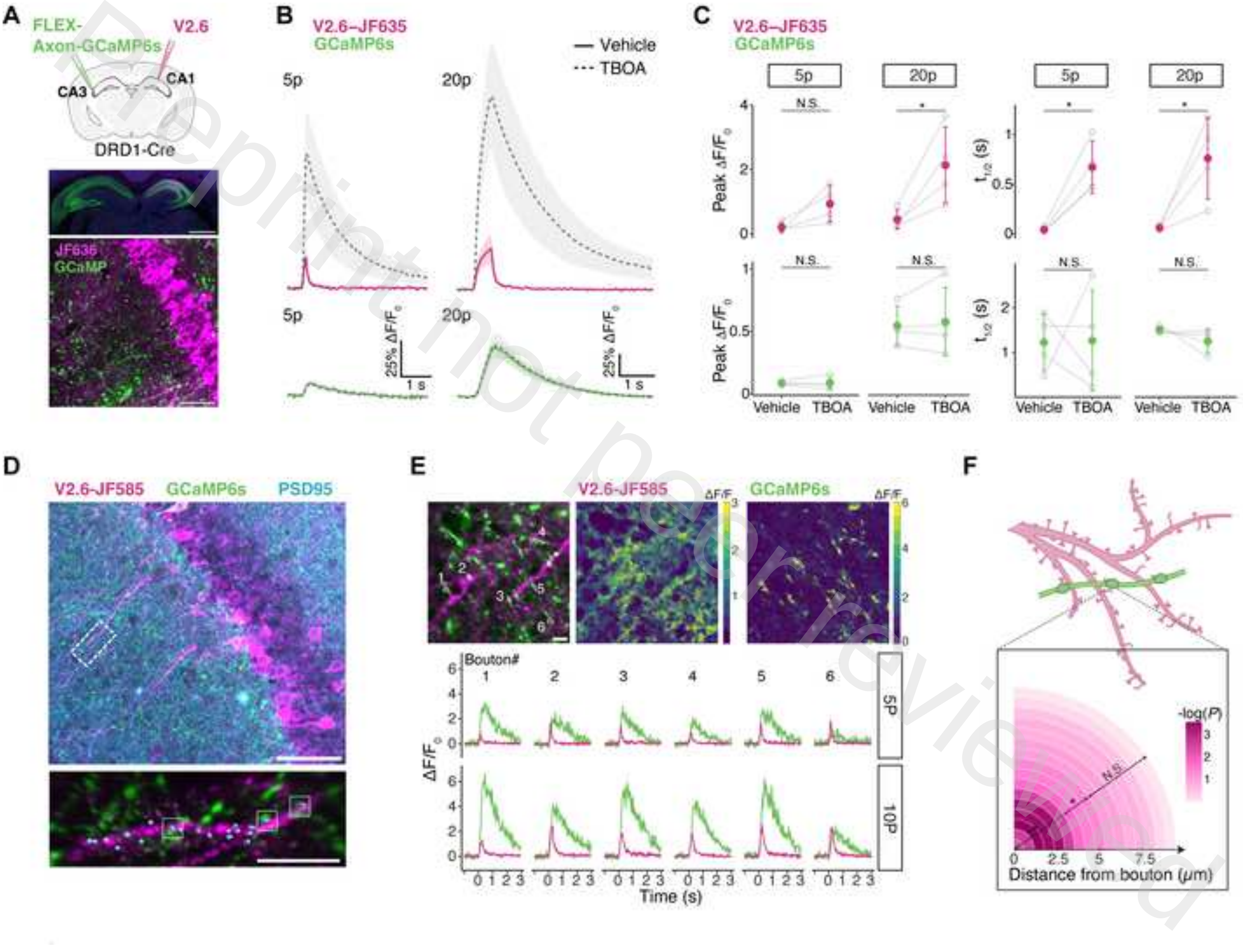
A
FLEX-
Axon-GCaMP6s
V2.6
CA3
CA1
DRD1-Cre
JF635
GCaMP
B
V2.6–JF635
GCaMP6s
— Vehicle
--- TBOA
5p
20p
5p
20p
25% ΔF/F₀
1 s
25% ΔF/F₀
1 s
C
V2.6–JF635
GCaMP6s
5p
20p
5p
20p
N.S.
*
*
*
Peak ΔF/F₀
4
2
0
$t_{1/2}$ (s)
1
0.5
0
N.S.
N.S.
N.S.
N.S.
Peak ΔF/F₀
1
0.5
0
$t_{1/2}$ (s)
2
1
Vehicle
TBOA
Vehicle
TBOA
Vehicle
TBOA
Vehicle
TBOA
D
V2.6-JF585
GCaMP6s
PSD95
E
V2.6-JF585
ΔF/F
3
2
1
GCaMP6s
ΔF/F
6
4
2
0
1
2
3
4
5
6
Bouton#
1
2
3
4
5
6
5P
10P
ΔF/F₀
6
4
2
0
6
4
2
0
0 1 2 3
0 1 2 3
0 1 2 3
0 1 2 3
0 1 2 3
0 1 2 3
Time (s)
F
-log(P)
3
2
1
N.S.
*
0
2.5
5
7.5
Distance from bouton (μm)

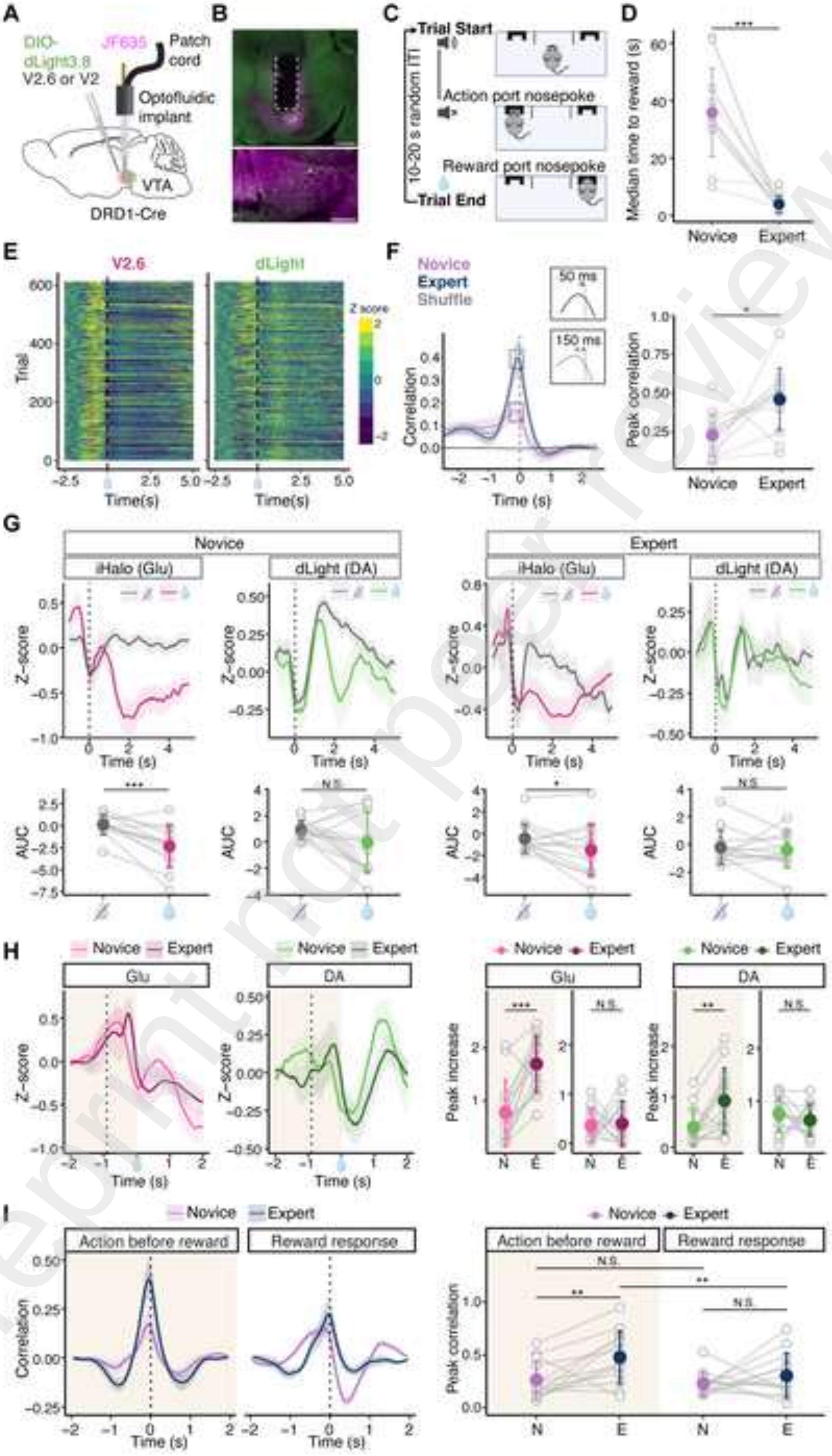
A
DIO-dLight3.8
V2.6 or V2
JF635
Patch cord
Optofluidic implant
VTA
DRD1-Cre
B
C
Trial Start
10-20 s random ITI
Action port nosepoke
Reward port nosepoke
Trial End
D
Median time to reward (s)
Novice
Expert
E
V2.6
dLight
Trial
Z score
Time(s)
F
Novice
Expert
Shuffle
50 ms
150 ms
Correlation
Time (s)
Peak correlation
G
Novice
Expert
iHalo (Glu)
dLight (DA)
Z-score
Time (s)
AUC
N.S.
H
Novice
Expert
Glu
DA
Z-score
Time (s)
Peak increase
N
E
I
Action before reward
Reward response
Correlation
Time (s)
Peak correlation
N.S.

Sensor	Dye	Cell type	Affinity (EC50)	Saturated Dynamic Range (ΔF/F) (%)	S-slope (μM-1)
iHaloGluSnFR V2	JF635	HEK293T stable cells	1.1 ± 0.2 μM	203.9± 5.9%	185.4
iHaloGluSnFR V2.6	JF635	HEK293T stable cells	12.4 ± 3.3 μM	720.8± 45.2%	58.1
iHaloGluSnFR V2.7b	JF635	HEK293T stable cells	84.6 ± 25.2 μM	1470± 117%	17.4
iHaloGluSnFR V2	JF585	HEK293T stable cells	0.98 ± 0.9 μM	25.2± 3.9%	25.7
iHaloGluSnFR V2.6	JF585	HEK293T stable cells	0.77 ± 0.3 μM	143.6± 9.5%	186.5
iHaloGluSnFR V2.7b	JF585	HEK293T stable cells	6.2 ± 1.2 μM	331.9± 11.3%	53.5
iHaloGluSnFR V2	JF646	HEK293T stable cells	0.79 ± 0.70 μM	14.0± 2.0%	17.7
iHaloGluSnFR V2.6	JF646	HEK293T stable cells	4.3 ± 1.1 μM	164.4± 9.4%	38.2
iHaloGluSnFR V2.7b	JF646	HEK293T stable cells	10.0 ± 2.6 μM	161.5± 8.4%	16.2
iHaloGluSnFR V2	JF635	E18 Hippocampal Neurons	4.8 ± 3.4 μM	285.1± 29.6%	59.4
iHaloGluSnFR V2.6	JF635	E18 Hippocampal Neurons	13.4 ± 4.0 μM	447.9± 26.9%	33.4
iHaloGluSnFR V2.7b	JF635	E18 Hippocampal Neurons	125.7 ± 28.9 μM	1371.5± 87.0%	10.9
iHaloGluSnFR V2	JF585	E18 Hippocampal Neurons	1.8 ± 0.7 μM	80.8± 5.3%	69.8
iHaloGluSnFR V2.6	JF585	E18 Hippocampal Neurons	13.4 ± 5.2 μM	91.1± 7.1%	6.8
iHaloGluSnFR V2.7b	JF585	E18 Hippocampal Neurons	21.6 ± 6.5 μM	361.8± 28.1%	16.8

Table S1. Titration data in HEK293T stable cell lines or AAV-transduced neurons. Shown as mean ± SEM.

Table S2

Sensor	Dye	1 AP peak ΔF/F	1 AP decay $t_{1/2}$	1 AP rise $t_{1/2}$	1 AP peak SNR	5 AP peak ΔF/F	5 AP peak SNR	10 AP peak ΔF/F	10 AP peak SNR	20 AP peak ΔF/F	20 AP peak SNR
iHaloGluSnFR V2	JF635	6.7 ± 0.9 %	642 ± 60.6 ms	≤ 30.5 ± 1.9 ms	12.0 ± 2.0	30.4 ± 4.5 %	52.4 ± 10.9	49.3 ± 8.0 %	79.9 ± 16.8	75.4 ± 13.6%	115.1 ± 25.6
iHaloGluSnFR V2.6	JF635	10.9 ± 1.4 %	86.0 ± 14.4 ms	≤ 24.7 ± 0.7 ms	13.4 ± 1.6	33.5 ± 3.5 %	39.4 ± 4.3	40.8 ± 3.9 %	48.8 ± 4.6	51.3 ± 4.8%	62.8 ± 6.6
iHaloGluSnFR V2.7b	JF635	6.0 ± 1.7 %	24.0 ± 3.5 ms	≤ 22.7 ± 1.3 ms	7.2 ± 1.5	12.0 ± 2.5 %	14.0 ± 2.4	14.3 ± 3.0 %	16.3 ± 2.7	18.2 ± 4.0%	23.2 ± 4.8
iHaloGluSnFR V2	JF585	20.4 ± 3.0 %	731± 29.9 ms	≤ 24 ms	44.1 ± 6.5	43.0 ± 4.3 %	87.2 ± 8.8	52.0 ± 4.4 %	99.7 ± 8.4	61.7 ± 4.6%	131.9 ± 9.5
iHaloGluSnFR V2.6	JF585	23.0 ± 3.2 %	97.4± 3.2 ms	≤ 24 ms	36.7 ± 5.7	60.6 ± 7.5 %	86.8 ± 9.4	70.5 ± 8.8 %	110.5 ± 13.0	78.8 ± 9.9%	121.0 ± 15.0
iHaloGluSnFR V2.7b	JF585	33.9 ± 6.1 %	20.4± 1.7 ms	≤ 24 ms	54.3 ± 10.3	47.5 ± 7.5 %	75.7 ± 12.7	47.5 ± 6.8 %	74.9 ± 12.1	51.8 ± 7.1%	85.1 ± 12.5
iHaloGluSnFR V2	JF646	2.5 ± 0.5 %	861± 137 ms	≤ 44.0 ± 6.7 ms	6.3 ± 1.0	8.0 ± 1.2 %	16.4 ± 1.9	12.1 ± 1.4 %	23.9 ± 2.5	17.0 ± 1.7%	35.8 ± 3.4
iHaloGluSnFR V2.6	JF646	10.3 ± 4.1 %	638 ± 54.5 ms	≤ 30.9 ± 2.4 ms	20.1 ± 8.0	31.4 ± 9.4 %	59.5 ± 19.3	43.1 ± 11.5 %	76.7 ± 20.5	55.6 ± 11.9%	107.9 ± 29.8

Table S2. AAV-transduced neuron whole field stimulation characterization. Shown as mean ± SEM.

Table S3

Sensor	Dye	Region	1 pulse peak $\Delta F/F$	1 pulse decay $t_{1/2}$	2 pulse peak $\Delta F/F$	2 pulse decay $t_{1/2}$	5 pulse peak $\Delta F/F$	5 pulse decay $t_{1/2}$	10 pulse peak $\Delta F/F$	10 pulse decay $t_{1/2}$	20 pulse peak $\Delta F/F$	20 pulse decay $t_{1/2}$
iHaloGluSnFR V2	JF635	HPC	7.7 ± 4.3 %	377.9 ± 193.0 ms	17.0 ± 9.6 %	426.1 ± 166.8 ms	54.3 ± 23.1 %	456.4 ± 73.8 ms	99.2 ± 32.7 %	463.1 ± 51.2 ms	139.6 ± 55.6 %	517.8 ± 90.8 ms
iHaloGluSnFR V2	JF635	DLS	5.3 ± 2.8 %	289.5 ± 177.0 ms	12.8 ± 7.8 %	323.9 ± 183.4 ms	29.0 ± 13.5 %	388.5 ± 117.0 ms	42.8 ± 18.4 %	459.4 ± 121.0 ms	52.9 ± 21.4 %	588.6 ± 87.9 ms
iHaloGluSnFR V2.6	JF635	M1	37.3 ± 16.3 %	40.4 ± 20.8 ms	67.4 ± 25.3 %	38.0 ± 16.2 ms	107.4 ± 33.9 %	41.7 ± 13.0 ms	111.0 ± 33.1 %	51.2 ± 17.9 ms	114.9 ± 39.1 %	57.1 ± 20.0 ms
iHaloGluSnFR V2.6	JF635	DLS	14.3 ± 6.3 %	47.3 ± 6.3 ms	30.3 ± 9.0 %	42.5 ± 20.2 ms	54.6 ± 18.1 %	36.5 ± 14.3 ms	56.7 ± 17.2 %	96.8 ± 81.1 ms	61.6 ± 19.2 %	80.7 ± 74.2 ms
iHaloGluSnFR V2.6	JF635	HPC	3.8 ± 1.5 %	NA: R2 of fit<0.7	9.2 ± 5.0 %	NA: R2 of fit<0.7	29.6 ± 16.0 %	36.0 ± 13.6 ms	47.6 ± 31.9 %	73.0 ± 83.1 ms	61.7 ± 40.1 %	91.6 ± 109.6 ms
iHaloGluSnFR V2.6	JF585	HPC	9.3 ± 7.1 %	73.3 ± 27.8 ms	34.0 ± 28.1 %	71.5 ± 2.1 ms	86.7 ± 60.6 %	80.5 ± 5.8 ms	115.1 ± 70.1 %	129.8 ± 115.7 ms	130.9 ± 72.5 %	101.2 ± 32.2 ms

Table S3. 2-photon acute slice stimulation characterization of iHaloGluSnFR. Shown as mean ± SD.

Table S4

Bouton index	Total quanta (for 50 APs)	Pr (quanta/AP)	PPR
1	23.03	0.46	1.28600386
2	26.57	0.53	1.11439004
3	14.69	0.29	0.86979977
4	21.23	0.42	1.18074668
5	64.25	1.28	1.0500839
6	44.94	0.9	1.27881008
7	68.09	1.36	1.02186945
8	41.62	0.83	0.8799558
9	41.25	0.83	1.11111641
10	20.75	0.42	1.17427503
11	10.04	0.2	0
12	25.49	0.51	0.83395424
13	34.68	0.69	1.02344102
14	37.79	0.76	1.37012533
15	35.62	0.71	1.22271697
16	24.02	0.48	0.76713933
17	22.82	0.46	0.76164903
18	15.68	0.31	1.42177613
19	23.65	0.47	0.98772026
20	35.67	0.71	1.32320895
21	49.28	0.99	0.92104842
22	26.48	0.53	0.91928517
23	30.41	0.61	1.5578495
24	54.04	1.08	0.97881056
25	14.59	0.29	0
26	36.68	0.73	0.65817228
27	47.18	0.94	1.18932506
28	35.26	0.71	1.30293938
29	46.85	0.94	0.82232895
30	10.95	0.22	0.44560994
31	32.1	0.64	1.18680155
32	37.34	0.75	0.89051838
33	55.15	1.1	0.81634778
34	29.87	0.6	0.85583073
35	33.82	0.68	1.11971638
36	18.09	0.36	0.59760731
37	60.78	1.22	0.96211872
38	7.76	0.16	2
39	11.26	0.23	1.20680301
40	4.19	0.08	0.88233296
41	4.68	0.09	2
42	6.8	0.14	1.59685806
43	5.16	0.1	1.27684555
44	3.45	0.07	No release
45	4.25	0.09	0.66681567
46	3.64	0.07	No release
47	4.09	0.08	1.09023012
48	10.83	0.22	1.18748486
49	6.95	0.14	0.7955229
50	23.11	0.46	1.22799621
51	14.93	0.3	0.74041614
52	21.29	0.43	1.36173482
53	2.5	0.05	2
54	14.77	0.3	0.60605854
55	11.72	0.23	0.93100947

56	15.24	0.3	0.84714078
57	21.33	0.43	0.54421778
58	20.38	0.41	0.94022468
59	21.32	0.43	0.94092942
60	11.34	0.23	0
61	25.89	0.52	0.48280563
62	0.92	0.02	0.86160106
63	6.44	0.13	1.01447725
64	4.87	0.1	No release
65	26	0.52	1.33038075
66	14.77	0.3	0.7184588
67	24.61	0.49	1.55862681
68	5.96	0.12	0.51197236
69	48.97	0.98	1.15417497
70	28.5	0.57	1.24186212
71	37.44	0.75	0.78811102
72	26.19	0.52	0.99786673
73	17.83	0.36	0.78408557
74	34.11	0.68	0.76881905
75	20.53	0.41	0.65954839
76	4.85	0.1	0
77	7.05	0.14	1.78852923
78	3.25	0.06	No release
79	1.71	0.03	No release
80	6.86	0.14	No release
81	21.06	0.42	0.27193554
82	1.04	0.02	No release
83	6.36	0.13	0.27024815
84	4.17	0.08	No release
85	6.58	0.13	0.33180838
86	3.87	0.08	No release
87	3.35	0.07	2
88	2.39	0.05	0.99141942
89	2.99	0.06	2
90	9.32	0.19	No release
91	4.66	0.09	0.77668556
92	7.58	0.15	2
93	5.35	0.11	2
94	7.32	0.15	0.57337995
95	17.75	0.35	0.87711257
96	8.68	0.17	1.63706006
97	30.64	0.61	0.79574751
98	16.01	0.32	2
99	5.38	0.11	0.84926629
100	18.8	0.38	1.27190102
101	19.98	0.4	0.86563621
102	5.47	0.11	0.71857498
103	6.11	0.12	2
104	2.17	0.04	1.1807849
105	17.44	0.35	1.3347272
106	3.4	0.07	No release
107	3.33	0.07	2
108	1.14	0.02	2
109	5.54	0.11	1.39801896
110	9.73	0.19	0
111	19.91	0.4	1.31778529

112	4.87	0.1	1.78263207
113	0.86	0.02	2
114	14.27	0.29	2
115	1.08	0.02	No release
116	2.11	0.04	1.62149645
117	4.81	0.1	2
118	8	0.16	0.34306095
119	20.22	0.4	2
120	1.67	0.03	0.69079841

Table S4. Bouton release profile of all boutons labeled in Figure 3B, including total quanta released, release rate, and optical paired-pulse ratio.

Supplemental Data: sequence

```
Consensus
1. V0 PDGFR
2. V2 GPI
3. V2.6 GPI
4. V2.7b GPI

IgK leader GltI cpHaloTag Myc
Transmembrane domain

  METDTLLLWVLLLWVPGSTGDRSAAGSTLDKIAKNGVIVVGHRESSVPFSYYDN--KVVGYSQDYSNAIV
           10        20        30        40        50        60        70
1 METDTLLLWVLLLWVPGSTGDRSAAGSTLDKIAKNGVIVVGHRESSVPFSYYDNQQKVVGYSQDYSNAIV  70
2 METDTLLLWVLLLWVPGSTGDRSAAGSTLDKIAKNGVIVVGHRESSVPFSYYDNQQKVVGYSQDYSNAIV  70
3 METDTLLLWVLLLWVPGSTGDRSAAGSTLDKIAKNGVIVVGHRESSVPFSYYDNHAKVVGYSQDYSNAIV  70
4 METDTLLLWVLLLWVPGSTGDRSAAGSTLDKIAKNGVIVVGHRESSVPFSYYDNHAKVVGYSQDYSNAIV  70

  EAVKKKLNKPDLQVKLIPITSQNRIPLLQNGTFDFECGSTTNNVERQKQAAFSDTIFVVGTRLLTKKGGD
           80        90       100       110       120       130       140
1 EAVKKKLNKPDLQVKLIPITSQNRIPLLQNGTFDFECGSTTNNVERQKQAAFSDTIFVVGTRLLTKKGGD  140
2 EAVKKKLNKPDLQVKLIPITSQNRIPLLQNGTFDFECGSTTNNVERQKQAAFSDTIFVVGTRLLTKKGGD  140
3 EAVKKKLNKPDLQVKLIPITSQNRIPLLQNGTFDFECGSTTNNVERQKQAAFSDTIFVVGTRLLTKKGGD  140
4 EAVKKKLNKPDLQVKLIPITSQNRIPLLQNGTFDFECGSTTNNVERQKQAAFSDTIFVVGTRLLTKKGGD  140

  IKDFANLKDKAVVVTSGTTSEVLLNKLNEEQKMNMRIISAKDHGDSFRTLESGRAVAFMMDD-LLAGERA
          150       160       170       180       190       200       210
1 IKDFANLKDKAVVVTSGTTSEVLLNKLNEEQKMNMRIISAKDHGDSFRTLESGRAVAFMMDDVLLAGERA  210
2 IKDFANLKDKAVVVTSGTTSEVLLNKLNEEQKMNMRIISAKDHGDSFRTLESGRAVAFMMDDSLLAGERA  210
3 IKDFANLKDKAVVVTSGTTSEVLLNKLNEEQKMNMRIISAKDHGDSFRTLESGRAVAFMMDDSLLAGERA  210
4 IKDFANLKDKAVVVTSGTTSEVLLNKLNEEQKMNMRIISAKDHGDSFRTLESGRAVAFMMDDVLLAGERA  210

  KAKKPDNWEIVGKPQSQEAYGCMLRKDDPQFKKLMDDTIAQVQTSGEAEKWFDKWFKNPILW-RETFQAF
          220       230       240       250       260       270       280
1 KAKKPDNWEIVGKPQSQEAYGCMLRKDDPQFKKLMDDTIAQVQTSGEAEKWFDKWFKNPILVARETFQAF  280
2 KAKKPDNWEIVGKPQSQEAYGCMLRKDDPQFKKLMDDTIAQVQTSGEAEKWFDKWFKNPILWARETFQAF  280
3 KAKKPDNWEIVGKPQSQEAYGCMLRKDDPQFKKLMDDTIAQVQTSGEAEKWFDKWFKNPILWGRETFQAF  280
4 KAKKPDNWEIVGKPQSQEAYGCMLRKDDPQFKKLMDDTIAQVQTSGEAEKWFDKWFKNPILWGRETFQAF  280

  RTTDVGRKLIIDQNVFIEGTLPMGVVRPLTEVEMDHYREPFLNPVDREPLWRFPNELPIAGEPANIVALV
          290       300       310       320       330       340       350
1 RTTDVGRKLIIDQNVFIEGTLPMGVVRPLTEVEMDHYREPFLNPVDREPLWRFPNELPIAGEPANIVALV  350
2 RTTDVGRKLIIDQNVFIEGTLPMGVVRPLTEVEMDHYREPFLNPVDREPLWRFPNELPIAGEPANIVALV  350
3 RTTDVGRKLIIDQNVFIEGTLPMGVVRPLTEVEMDHYREPFLNPVDREPLWRFPNELPIAGEPANIVALV  350
4 RTTDVGRKLIIDQNVFIEGTLPMGVVRPLTEVEMDHYREPFLNPVDREPLWRFPNELPIAGEPANIVALV  350

  EEYMDWLHQSPVPKLLFWGTPGVLIPPAEAARLAKSLPNCKAVDIGPGLNLLQEDNPDLIGSEIARWLST
          360       370       380       390       400       410       420
1 EEYMDWLHQSPVPKLLFWGTPGVLIPPAEAARLAKSLPNCKAVDIGPGLNLLQEDNPDLIGSEIARWLST  420
2 EEYMDWLHQSPVPKLLFWGTPGVLIPPAEAARLAKSLPNCKAVDIGPGLNLLQEDNPDLIGSEIARWLST  420
3 EEYMDWLHQSPVPKLLFWGTPGVLIPPAEAARLAKSLPNCKAVDIGPGLNLLQEDNPDLIGSEIARWLST  420
4 EEYMDWLHQSPVPKLLFWGTPGVLIPPAEAARLAKSLPNCKAVDIGPGLNLLQEDNPDLIGSEIARWLST  420

  LEISGGGTGGSGGTGGSGGTGGSMAEIGTGFPFDPHYVEVLGERMHYVDVGPRDGTPVLFLHGNPTSSYV
          430       440       450       460       470       480       490
1 LEISGGGTGGSGGTGGSGGTGGSMAEIGTGFPFDPHYVEVLGERMHYVDVGPRDGTPVLFLHGNPTSSYV  490
2 LEISGGGTGGSGGTGGSGGTGGSMAEIGTGFPFDPHYVEVLGERMHYVDVGPRDGTPVLFLHGNPTSSYV  490
3 LEISGGGTGGSGGTGGSGGTGGSMAEIGTGFPFDPHYVEVLGERMHYVDVGPRDGTPVLFLHGNPTSSYV  490
4 LEISGGGTGGSGGTGGSGGTGGSMAEIGTGFPFDPHYVEVLGERMHYVDVGPRDGTPVLFLHGNPTSSYV  490

  WRNIIPHVAPTHRCIAPDLIGMGKSDKPDLGYFFDDHVRFMDAFIEALGLEEVVLVIHDWGSALGFHWAK
          500       510       520       530       540       550       560
1 WRNIIPHVAPTHRCIAPDLIGMGKSDKPDLGYFFDDHVRFMDAFIEALGLEEVVLVIHDWGSALGFHWAK  560
2 WRNIIPHVAPTHRCIAPDLIGMGKSDKPDLGYFFDDHVRFMDAFIEALGLEEVVLVIHDWGSALGFHWAK  560
3 WRNIIPHVAPTHRCIAPDLIGMGKSDKPDLGYFFDDHVRFMDAFIEALGLEEVVLVIHDWGSALGFHWAK  560
4 WRNIIPHVAPTHRCIAPDLIGMGKSDKPDLGYFFDDHVRFMDAFIEALGLEEVVLVIHDWGSALGFHWAK  560

  RNPERVKGIAFMEFIRPIPTWDEWPE-NGLNMNFELSDEMKALFKEPNDKALKLQVDEQKLISEEDLSDN
          570       580       590       600       610       620       630
1 RNPERVKGIAFMEFIRPIPTWDEWPEFNPLNMNFELSDEMKALFKEPNDKALKLQVDEQKLISEEDLNAV  630
2 RNPERVKGIAFMEFIRPIPTWDEWPEFNGLNMNFELSDEMKALFKEPNDKALKLQVDEQKLISEEDLSDN  630
3 RNPERVKGIAFMEFIRPIPTWDEWPEGNGLNMNFELSDEMKALFKEPNDKALKLQVDEQKLISEEDLSDN  630
4 RNPERVKGIAFMEFIRPIPTWDEWPEGIGLNMNFELSDEMKALFKEPNDKALKLQVDEQKLISEEDLSDN  630

  DYGKDGLAGASGGRRNGAI---TVLSFITFYVAAFMVLL---------
          640       650       660       670
1 GQDTQEVIVVPHSLPFKVVVISAILALVVLTIISLIILIMLWQKKPR  677
2 DYGKDGLAGASGGRRNGAI---TVLSFITFYVAAFMVLL---------  666
3 DYGKDGLAGASGGRRNGAI---TVLSFITFYVAAFMVLL---------  666
4 DYGKDGLAGASGGRRNGAI---TVLSFITFYVAAFMVLL---------  666
```

Figure S1

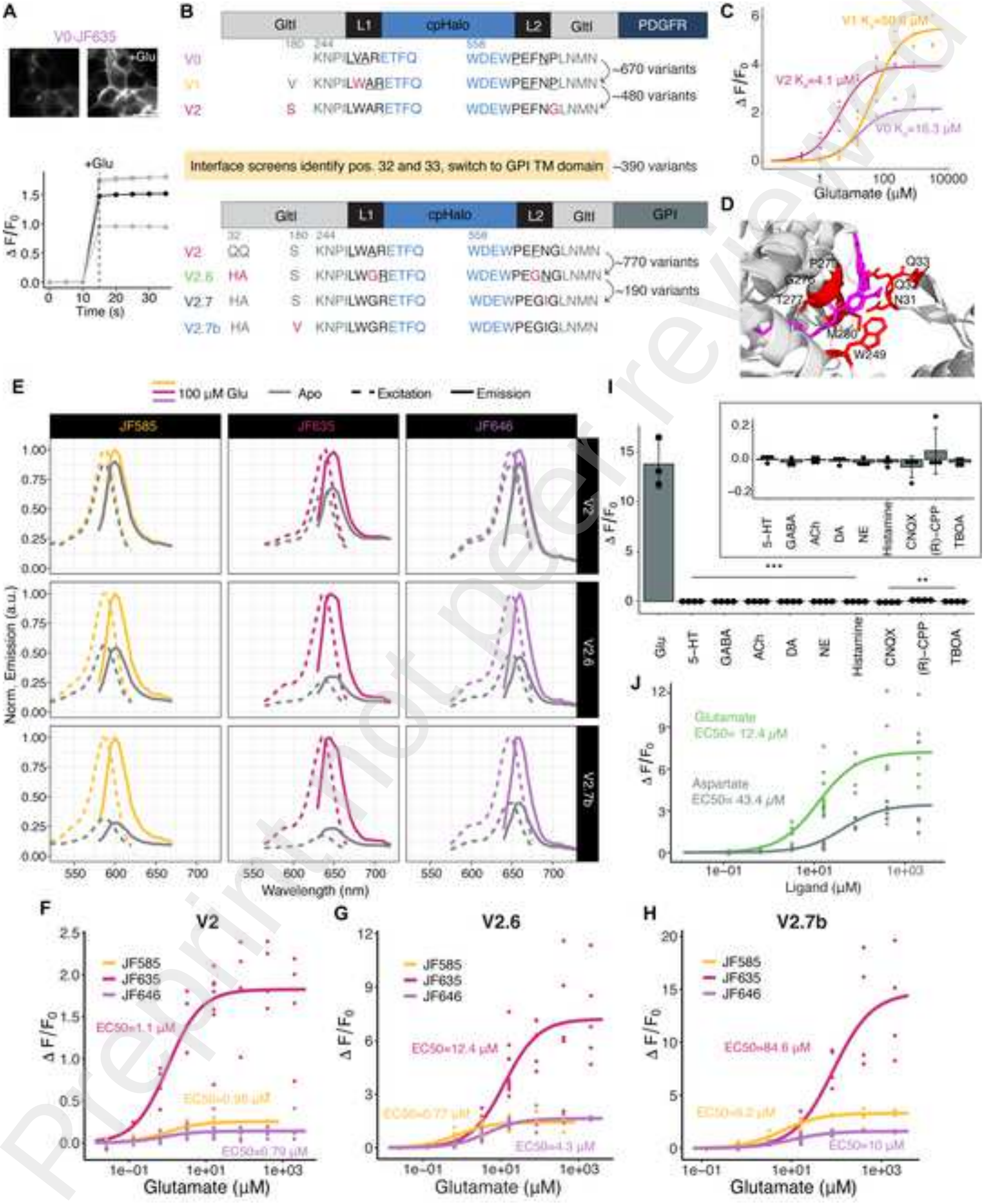
A
V0-JF635
+Glu
+Glu
1.5
1.0
0.5
0.0
Δ F/F0
0
10
20
30
Time (s)
B
Gltl
L1
cpHalo
L2
Gltl
PDGFR
180
244
558
V0
KNPILVARETFQ
WDEWPEFNPLNMN
V1
V
KNPILWARETFQ
WDEWPEFNPLNMN
V2
S
KNPILWARETFQ
WDEWPEFNGLNMN
~670 variants
~480 variants
Interface screens identify pos. 32 and 33, switch to GPI TM domain
~390 variants
Gltl
L1
cpHalo
L2
Gltl
GPI
32
180
244
558
V2
QQ
S
KNPILWARETFQ
WDEWPEFNGLNMN
V2.6
HA
S
KNPILWGRETFQ
WDEWPEGNGLNMN
V2.7
HA
S
KNPILWGRETFQ
WDEWPEGIGLNMN
V2.7b
HA
V
KNPILWGRETFQ
WDEWPEGIGLNMN
~770 variants
~190 variants
C
V1 K_d=50.8 μM
V2 K_d=4.1 μM
V0 K_d=16.3 μM
Δ F/F0
0
2
4
6
1
100
10000
Glutamate (μM)
D
P277
G276
T277
M280
W249
Q33
Q32
N31
E
100 μM Glu
Apo
Excitation
Emission
JF585
JF635
JF646
V2
V2.6
V2.7b
Norm. Emission (a.u.)
0.00
0.25
0.50
0.75
1.00
550
600
650
700
Wavelength (nm)
F
V2
JF585
JF635
JF646
EC50=1.1 μM
EC50=0.98 μM
EC50=0.79 μM
Δ F/F0
0.0
0.5
1.0
1.5
2.0
2.5
1e−01
1e+01
1e+03
Glutamate (μM)
G
V2.6
JF585
JF635
JF646
EC50=12.4 μM
EC50=0.77 μM
EC50=4.3 μM
Δ F/F0
0
3
6
9
12
1e−01
1e+01
1e+03
Glutamate (μM)
H
V2.7b
JF585
JF635
JF646
EC50=84.6 μM
EC50=4.2 μM
EC50=10 μM
Δ F/F0
0
5
10
15
20
1e−01
1e+01
1e+03
Glutamate (μM)
I
Δ F/F0
0
5
10
15
***
**
Glu
5−HT
GABA
ACh
DA
NE
Histamine
CNQX
(R)−CPP
TBOA
0.2
0.0
−0.2
5−HT
GABA
ACh
DA
NE
Histamine
CNQX
(R)−CPP
TBOA
J
Glutamate
EC50= 12.4 μM
Aspartate
EC50= 43.4 μM
Δ F/F0
0
3
6
9
12
1e−01
1e+01
1e+03
Ligand (μM)

Figure S2

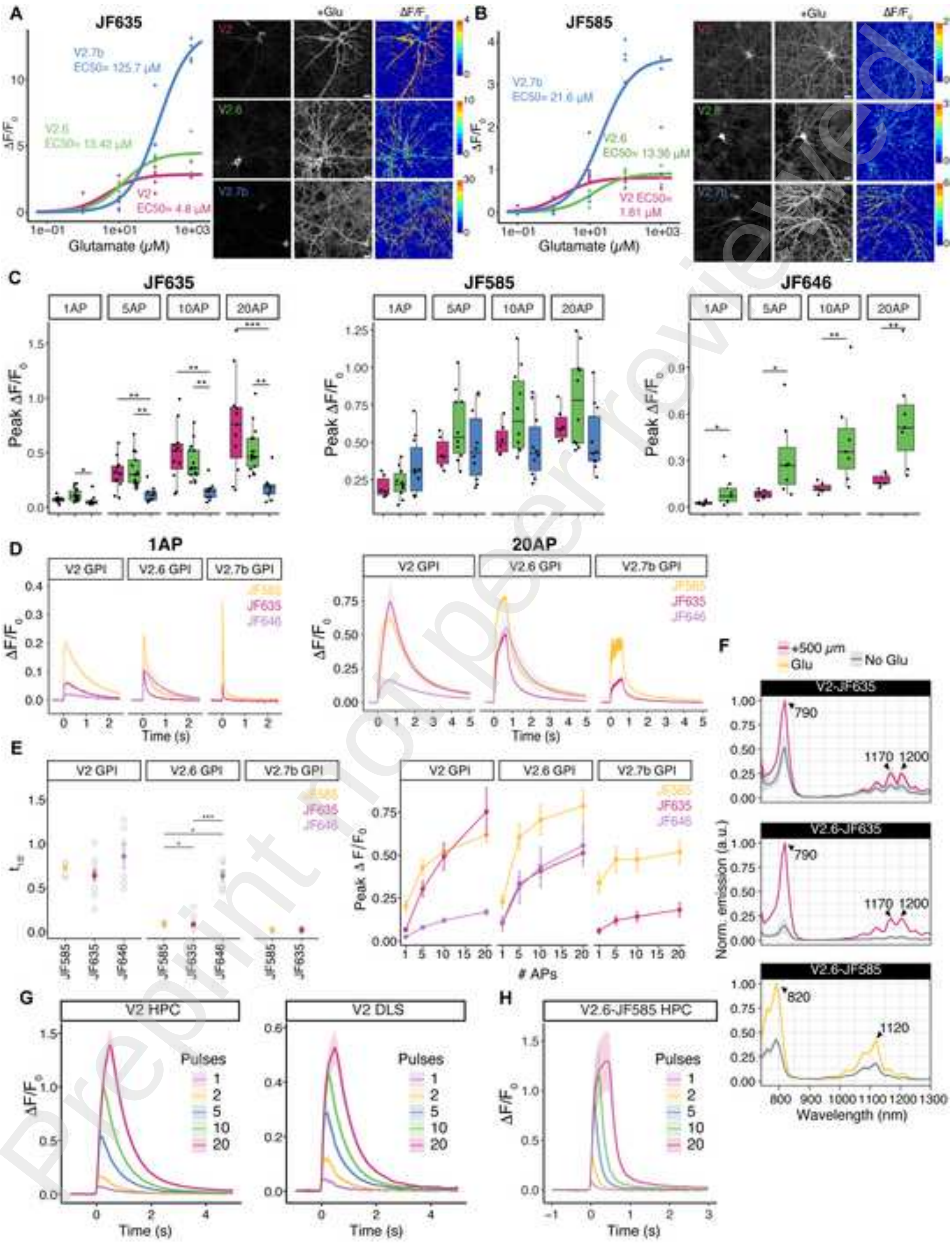
A
JF635
V2.7b
EC50= 125.7 µM
V2.6
EC50= 13.42 µM
V2
EC50= 4.8 µM
ΔF/F₀
Glutamate (µM)
1e-01
1e+01
1e+03
+Glu
ΔF/F₀
B
JF585
V2.7b
EC50= 21.6 µM
V2.6
EC50= 13.36 µM
V2 EC50=
1.61 µM
C
JF635
JF585
JF646
1AP
5AP
10AP
20AP
Peak ΔF/F₀
D
1AP
20AP
V2 GPI
V2.6 GPI
V2.7b GPI
JF585
JF635
JF646
ΔF/F₀
Time (s)
E
t₁/₂
Peak ΔF/F₀
APs
F
+500 µm Glu
No Glu
V2-JF635
V2.6-JF635
V2.6-JF585
790
1170
1200
820
1120
Norm. emission (a.u.)
Wavelength (nm)
G
V2 HPC
V2 DLS
Pulses
1
2
5
10
20
ΔF/F₀
Time (s)
H
V2.6-JF585 HPC

Figure S3

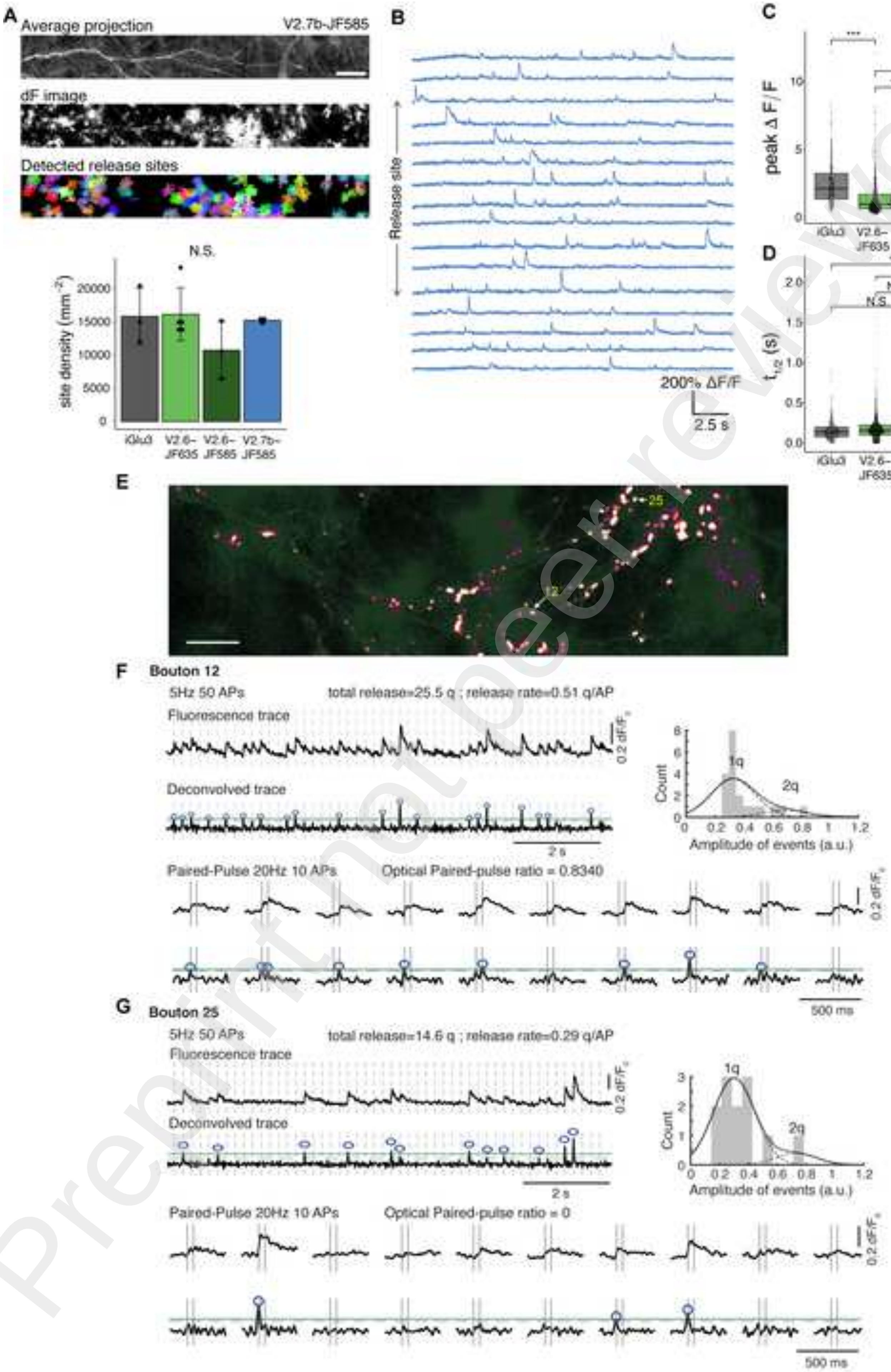
A
Average projection
V2.7b-JF585
dF image
Detected release sites
N.S.
site density (mm^{-2})
20000
15000
10000
5000
0
iGlu3
V2.6-JF635
V2.6-JF585
V2.7b-JF585
B
Release site
200% ΔF/F
2.5 s
C
peak Δ F / F
10
5
0
***
iGlu3
V2.6-JF635
V2.6-JF585
V2.7b-JF585
D
$t_{1/2}$ (s)
2.0
1.5
1.0
0.5
0.0
N.S.
***
E
25
12
F
Bouton 12
5Hz 50 APs
total release=25.5 q ; release rate=0.51 q/AP
Fluorescence trace
0.2 dF/F$_0$
Deconvolved trace
2 s
Count
8
6
4
2
0
1q
2q
Amplitude of events (a.u.)
0 0.2 0.4 0.6 0.8 1 1.2
Paired-Pulse 20Hz 10 APs
Optical Paired-pulse ratio = 0.8340
0.2 dF/F$_0$
500 ms
G
Bouton 25
5Hz 50 APs
total release=14.6 q ; release rate=0.29 q/AP
Fluorescence trace
0.2 dF/F$_0$
Deconvolved trace
2 s
Count
3
2
1
0
1q
2q
Amplitude of events (a.u.)
0 0.2 0.4 0.6 0.8 1 1.2
Paired-Pulse 20Hz 10 APs
Optical Paired-pulse ratio = 0
0.2 dF/F$_0$
500 ms

Figure S4

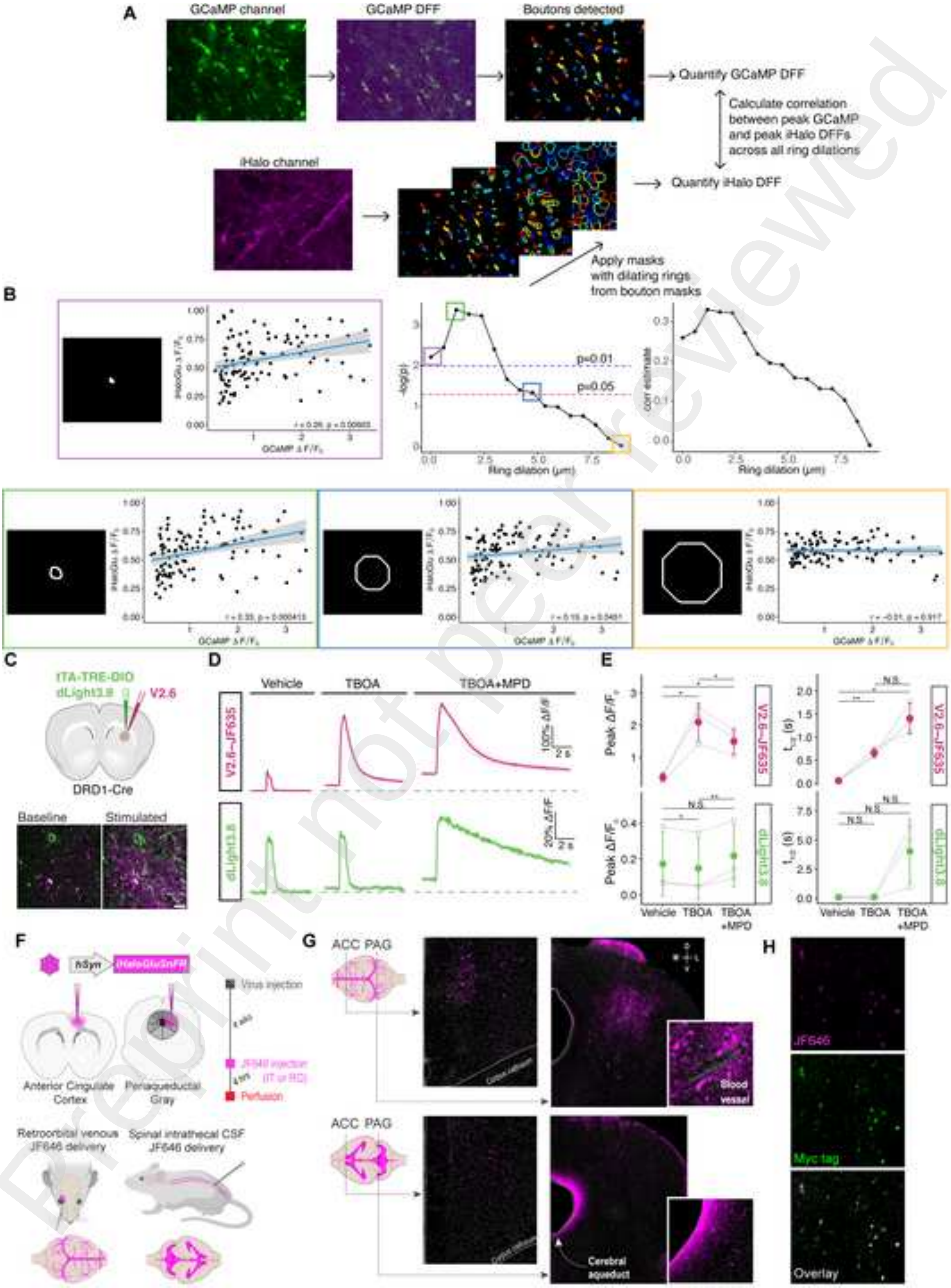
A
GCaMP channel
GCaMP DFF
Boutons detected
Quantify GCaMP DFF
Calculate correlation between peak GCaMP and peak iHalo DFFs across all ring dilations
iHalo channel
Quantify iHalo DFF
Apply masks with dilating rings from bouton masks
B
iHaloGlu Δ F/F₀
GCaMP Δ F/F₀
r = 0.26, p = 0.00603
-log(p)
p=0.01
p=0.05
Ring dilation (μm)
corr estimate
r = 0.33, p = 0.000415
r = 0.15, p = 0.0491
r = -0.01, p = 0.917
C
tTA-TRE-DIO dLight3.8
V2.6
DRD1-Cre
Baseline
Stimulated
D
Vehicle
TBOA
TBOA+MPD
V2.6–JF635
dLight3.8
100% ΔF/F
20% ΔF/F
2 s
E
Peak ΔF/F₀
t₁/₂ (s)
N.S.
Vehicle
TBOA
TBOA +MPD
F
hSyn
iHaloGluSnFR
Anterior Cingulate Cortex
Periaqueductal Gray
Virus injection
JF646 injection (IT or RO)
Perfusion
Retroorbital venous JF646 delivery
Spinal intrathecal CSF JF646 delivery
G
ACC PAG
Corpus callosum
Blood vessel
Cerebral aqueduct
H
JF646
Myc tag
Overlay

Figure S5

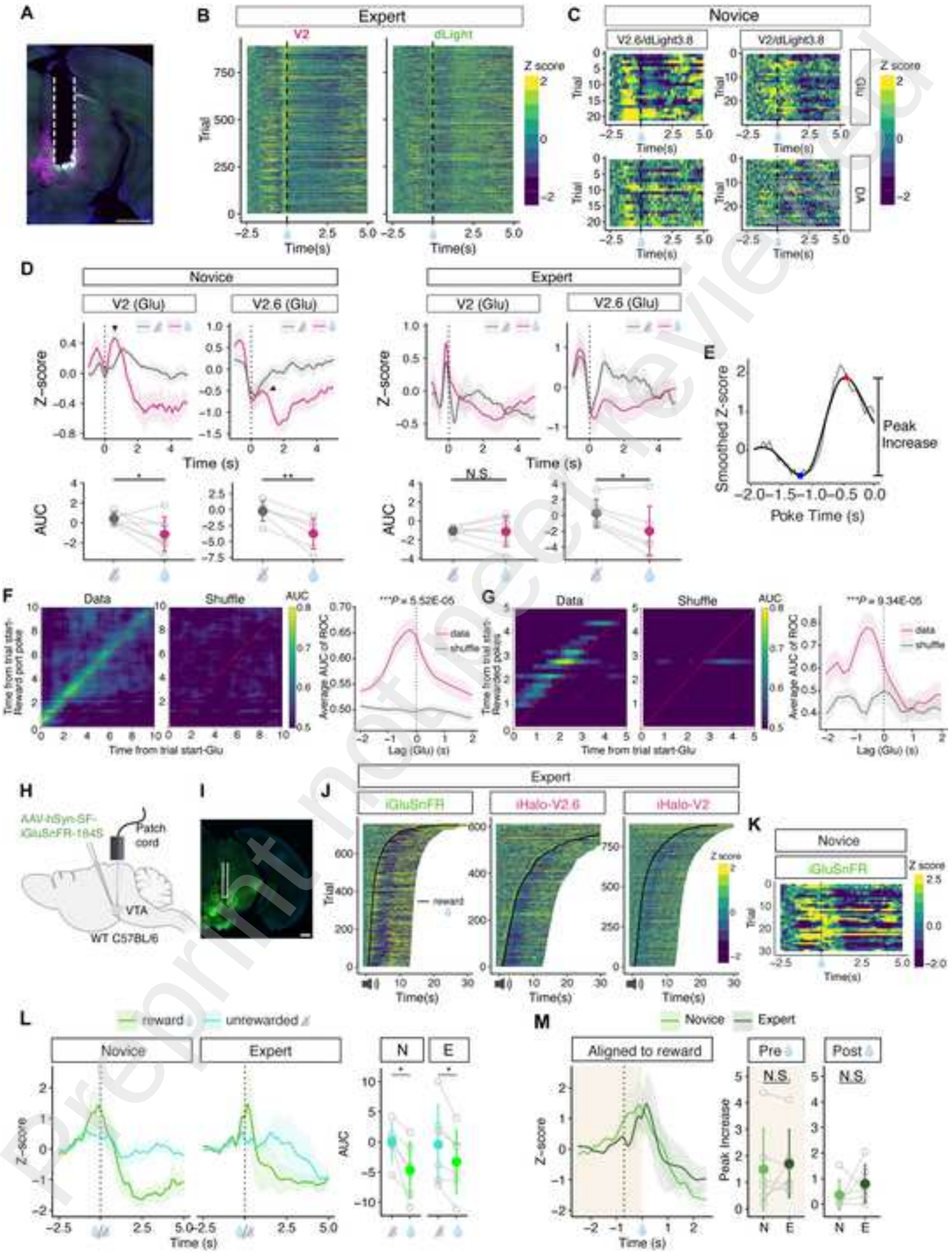
A
B
Expert
V2
dLight
Trial
750
500
250
0
-2.5
2.5
5.0
Time(s)
Z score
2
0
-2
C
Novice
V2.6/dLight3.8
V2/dLight3.8
Glu
DA
D
Novice
Expert
V2 (Glu)
V2.6 (Glu)
Z-score
Time (s)
AUC
*
**
N.S.
E
Smoothed Z-score
Peak Increase
Poke Time (s)
F
Data
Shuffle
AUC
Time from trial start-Reward port poke
Time from trial start-Glu
***P = 5.52E-05
Average AUC of ROC
data
shuffle
Lag (Glu) (s)
G
Time from trial start-Rewarded pokes
***P = 9.34E-05
H
AAV-hSyn-SF-iGluSnFR-184S
Patch cord
VTA
WT C57BL/6
I
J
Expert
iGluSnFR
iHalo-V2.6
iHalo-V2
reward
K
Novice
iGluSnFR
L
reward
unrewarded
Novice
Expert
N
E
M
Novice
Expert
Aligned to reward
Pre
Post
N.S.
Peak Increase

CELL PRESS DECLARATION OF INTERESTS POLICY

Transparency is essential for a reader's trust in the scientific process and for the credibility of published articles. At Cell Press, we feel that disclosure of competing interests is a critical aspect of transparency. Therefore, we require a "declaration of interests" section in which all authors disclose any financial or other interests related to the submitted work that (1) could affect or have the perception of affecting the author's objectivity or (2) could influence or have the perception of influencing the content of the article.

What types of articles does this apply to?

We require that you disclose competing interests for all submitted content by completing and submitting the form below. We also require that you include a "declaration of interests" section in the text of all articles even if there are no interests to declare.

What should I disclose?

We require that you and all authors disclose any personal financial interests (e.g., stocks or shares in companies with interests related to the submitted work or consulting fees from companies that could have interests related to the work), professional affiliations, advisory positions, board memberships (including membership on a journal's advisory board when publishing in that journal), or patent applications and/or registrations that are related to the subject matter of the contribution. As a guideline, you need to declare an interest for (1) any affiliation associated with a payment or financial benefit exceeding $10,000 p.a. or 5% ownership of a company or (2) research funding by a company with related interests. You do not need to disclose diversified mutual funds, 401ks, or investment trusts.

Authors should also disclose relevant financial interests of immediate family members. Cell Press uses the Public Health Service definition of "immediate family member," which includes spouse and dependent children.

Where do I declare competing interests?

Competing interests should be disclosed on this form as well as in a "declaration of interests" section in the manuscript. This section should include financial or other competing interests as well as affiliations that are not included in the author list. Examples of "declaration of interests" language include:

> "AUTHOR is an employee and shareholder of COMPANY."
> "AUTHOR is a founder of COMPANY and a member of its scientific advisory board."

NOTE: Primary affiliations should be included with the author list and do not need to be included in the "declaration of interests" section. Funding sources should be included in the "acknowledgments" section and also do not need to be included in the "declaration of interests" section. (A small number of front-matter article types do not include an "acknowledgments" section. For these articles, reporting of funding sources is not required.)

What if there are no competing interests to declare?

If you have no competing interests to declare, please note that in the "declaration of interests" section with the following wording:

> "The authors declare no competing interests."

April 12, 2024

CellPress

CELL PRESS DECLARATION OF INTERESTS FORM

If submitting materials via Editorial Manager, please complete this form and upload with your initial submission. Otherwise, please email as an attachment to the editor handling your manuscript.

Please complete each section of the form and insert any necessary "declaration of interests" statement in the text box at the end of the form. A matching statement should be included in a "declaration of interests" section in the manuscript.

Institutional affiliations

We require that you list the current institutional affiliations of all authors, including academic, corporate, and industrial, on the title page of the manuscript. ***Please select one of the following:***

☒ All affiliations are listed on the title page of the manuscript.

☐ I or other authors have additional affiliations that we have noted in the "declaration of interests" section of the manuscript and on this form below.

Funding sources

We require that you disclose all funding sources for the research described in this work. ***Please confirm the following:***

☒ All funding sources for this study are listed in the "acknowledgments" section of the manuscript.*

*A small number of front-matter article types do not include an "acknowledgments" section. For these, reporting funding sources is not required.

Competing financial interests

We require that authors disclose any financial interests and any such interests of immediate family members, including financial holdings, professional affiliations, advisory positions, board memberships, receipt of consulting fees, etc., that:

(1) could affect or have the perception of affecting the author's objectivity, *or*
(2) could influence or have the perception of influencing the content of the article.

Please select one of the following:

☐ We, the authors and our immediate family members, have no financial interests to declare.

☒ We, the authors, have noted any financial interests in the "declaration of interests" section of the manuscript and on this form below, and we have noted interests of our immediate family members.

April 12, 2024

Advisory/management and consulting positions

We require that authors disclose any position, be it a member of a board or advisory committee or a paid consultant, that they have been involved with that is related to this study. We also require that members of our journal advisory boards disclose their position when publishing in that journal. ***Please select one of the following:***

- ☒ We, the authors and our immediate family members, have no positions to declare and are not members of the journal's advisory board.
- ☐ The authors and/or their immediate family members have management/advisory or consulting relationships noted in the "declaration of interests" section of the manuscript and on this form below.

Patents

We require that you disclose any patent applications and/or registrations related to this work by any of the authors or their institutions. ***Please select one of the following:***

- ☐ We, the authors and our immediate family members, have no related patent applications or registrations to declare.
- ☒ We, the authors, have a patent application and/or registration related to this work, which is noted in the "declaration of interests" section of the manuscript and on this form below, and we have noted the patents of immediate family members.

Please insert any "declaration of interests" statements in this space. This exact text should also be included in the "declaration of interests" section of the manuscript. If no authors have a competing interest, please insert the text, "The authors declare no competing interests."

L.D.L is a scientific cofounder, shareholder, and consultant of Eikon Therapeutics. US Patent 9,933,417 describing azetidine-containing fluorophores and variant compositions (with inventor L.D.L) is assigned to HHMI.

☒ **On behalf of all authors, I declare that I have disclosed all competing interests related to this work. If any exist, they have been included in the "declaration of interests" section of the manuscript.**

April 12, 2024